

arXiv:1801.08238v1 [physics.ao-ph] 24 Jan 2018

# **Bernhard Haurwitz Memorial Lecture (2017): Potential Vorticity Aspects of Tropical Dynamics**

Wayne H. Schubert \*

*Department of Atmospheric Science, Colorado State University, Fort Collins, Colorado*

This paper is the textual material accompanying the 2017 Bernhard Haurwitz Memorial Lecture, delivered by the author on 28 June 2017, at a joint session of the American Meteorological Society's 21<sup>st</sup> Conference on Atmospheric and Oceanic Fluid Dynamics and 19<sup>th</sup> Conference on Middle Atmosphere (26–30 June 2017, Portland, OR).

\**Corresponding author:* Wayne H. Schubert, Department of Atmospheric Science, Colorado State University, Fort Collins, Colorado 80523  
E-mail: waynes@atmos.colostate.edu

## 1. Introduction

Bernhard Haurwitz (1905–1986) was one of the pioneers in atmospheric and oceanic fluid dynamics, commonly referred to as AOFD. While some of today's older generation had the good fortune of knowing Bernhard personally, or of being his colleague, perhaps most AOFD and middle atmosphere researchers know of his work through the Rossby–Haurwitz wave. George Platzman (1968) has provided an account of the somewhat intricate history of the Rossby–Haurwitz wave, during the half century 1890–1940. An expanded version of Platzman's skeletal history is given in Table 1.

As is customary, the history starts with the remarkable work of Pierre-Simon Laplace (1749–1827). During the years (1799–1827), about a century after Newton's *Philosophiæ Naturalis Principia Mathematica*, Laplace produced his monumental, five-volume<sup>1</sup> treatise entitled *Traité de mécanique céleste*, which discusses the orbits of the then-known planets (out to Uranus), comets, and moons. In addition, Laplace develops some of the principles of atmospheric and oceanic fluid dynamics. In Volume I (First Book, Chapter VIII, pages 194–238), Laplace begins his discussion of the motions of fluids. On pages 210–212 he considers the oscillations of a fluid mass surrounding a rotating spheroid. His equation (325) presents the three components of the vector equation of fluid motion, including the Coriolis terms<sup>2</sup> proportional to both the sine and cosine of the latitude. On page 228 Laplace pauses this discussion with the statement that “to determine the oscillations of the sea and the atmosphere, it is now only necessary to know the forces which act upon these two fluid masses, and to integrate the preceding differential equations, which will be done in the course of this work.” In Volume II (Fourth Book, Chapters I–V, pages 526–570), Laplace resumes his discussion of “The Oscillations of the Sea and Atmosphere,” formulating the required equations when there is gravitational attraction by the sun and the moon. Although Laplace had a good understanding of gravity waves, the discovery of planetary waves is not attributed to him, but rather to Margules (1893) and Hough (1897, 1898), who found that the solutions of Laplace's tidal equations could be divided into two classes we now call gravitational modes and rotational modes. Platzman's historical interpretation is as follows:

“Margules' investigation<sup>3</sup> of the tidal equations was the first in which the global planetary wave was explicitly studied from the standpoint of applications to meteorology. It was not taken up again from this point of view until the late 1920's and early 1930's when the Leipzig school<sup>4</sup> enlisted it in an attempt to find a theoretical basis for numerous empirical periodicities then believed to exist in meteorological data, ranging from a few days to 37 or more days. The principal theoretical outcome of these efforts was a paper by Haurwitz in 1937, in which Margules' calculations were extended and improved, using the more powerful methods developed by Hough. When in 1939 the (Rossby) trough formula was announced, Haurwitz saw its connection with the theory of oscillations of the second class that had come down from Margules and Hough, and through his own hands. He showed how the formula could be extended to allow for finite width, first on the  $\beta$ -plane (Haurwitz 1940a) and then on the sphere (Haurwitz 1940b). In the latter paper the westward-drift formula  $2\Omega/n(n+1)$  — first stated by Hough — was deduced directly for Rossby's prototype barotropic nondivergent atmosphere, rather than indirectly from the intricate context of Laplace's tidal equations.”

Since 1940, there have been hundreds of papers written on Rossby–Haurwitz waves. Table 1 lists the three classics written by Longuet-Higgins (1964, 1965, 1968, the latter of which provides a complete solution of Laplace's tidal equations, including mixed Rossby-gravity waves (also referred to as Yanai waves) and Kelvin waves. Thanks to the efforts of many, including Swartrauber and Kasahara (1985), Žagar et al. (2015), and Wang et al. (2016), the community has software available for computing the eigenvalues and eigenfunctions of Laplace's tidal equations.

In the mid-1930's while working on planetary scale problems, Haurwitz also began thinking about tropical cyclones.<sup>5</sup> Over the years, his interest focused on three topics: (i) The motion of binary tropical cyclones (1951); (ii) The height of tropical cyclones and of the eye (1935b, 1936c); (iii) The Ekman layer under curved air currents (1935a, 1935c, 1936b, 1936a). His work on topic (i) can be considered one of the first efforts at tropical cyclone track prediction using simple barotropic arguments. His work on topic (ii) was done before there were any relevant radiosonde

<sup>1</sup>Nathaniel Bowditch published English translations with extended commentary of the first four volumes from 1829–1839. Digital versions of these translations are available online at the Internet Archive.

<sup>2</sup>One wonders if the “Coriolis terms” should more accurately be called the “Laplace terms.”

<sup>3</sup>Haurwitz has provided an English translation of Margules' three part work entitled “Air Motions in a Rotating Spheroidal Shell”. See the reference list under Margules (1892, 1893a, 1893b).

<sup>4</sup>A history of the Leipzig school can be found in the book by Ehrmann and Wendisch 2013, written on the occasion of the 100th anniversary of the founding of the Geophysical Institute in 1913.

<sup>5</sup>Some very interesting aspects of the history and science of tropical cyclones (some before Haurwitz' time) are discussed in the book by Emanuel (2005).

TABLE 1. A skeletal chronology of the theory of planetary waves. This is a slight expansion of the chronology presented by Platzman (1968).

Regional Planetary Waves ( $\beta$ -Plane)	Global Planetary Waves (Sphere)
	Laplace (1799–1827)
	Margules (1892, 1893a,b)
	Hough (1897, 1898)
Ekman (1923, 1932)	
Bjerknes (1937)	
Rossby (1939, 1940)	
Haurwitz (1937, 1940a)	Haurwitz (1940b)
Longuet-Higgins (1964, 1965)	
Matsuno (1966)	
Blandford (1966)	
	Longuet-Higgins (1968)
	Swarztrauber and Kasahara (1985)

observations or aircraft penetrations and well before the era of weather radar and weather satellites. At the time, there was uncertainty about the depth of the circulation in tropical cyclones, with some arguing that the circulation extended upward only a few kilometers due in part to observations of rapid weakening during landfall. Using hydrostatic arguments Haurwitz showed that, unless the circulation extends up to at least 10 km, the associated temperature distribution is unreasonable. Of course, as radiosonde, aircraft, radar, and satellite data became available, he was proved correct. Haurwitz also commented on the “shape of the funnel”, which is often referred to as the “stadium effect” or the outward slope of the eyewall. A modern day example of this is shown in Fig. 1. Haurwitz’ work on topic (iii) had the goal of generalizing the planetary boundary layer solutions of Ekman and Taylor to allow the imposed pressure field to have curved isobars, making the solutions more relevant to tropical cyclones.<sup>6</sup> When asked by Platzman (1985) to explain what got him interested in this problem, Haurwitz replied: “I wanted to find an explanation why the hurricane has an eye. I had in mind that there should be something which comes directly out of the hydrodynamic equations, which tells you that the influx into the hurricane in the outer part has got to stop somewhere.” He was on the right track, and we shall return to this problem in section 5. However, we begin our discussion with some more recent concepts about the potential vorticity structure of tropical cyclones.

## 2. The formation of PV towers in tropical cyclones

It is sometimes said that a tropical cyclone consists of a mesoscale ( $\sim 100$  km) power plant with a synoptic scale ( $\sim 1000$  km) supporting structure (Ooyama 1982). Tropical cyclone track forecasting requires that we accurately model the synoptic scale supporting structure. The more difficult task of tropical cyclone intensity forecasting requires that we accurately model the mesoscale power plant. Although there is transient inertia-gravity wave activity in a tropical cyclone, the tropical cyclone vortex can be idealized to a balanced, PV phenomenon, with the balanced wind and mass fields invertible from the PV field. The PV is far from being materially conserved. With frictional effects confined primarily to a shallow boundary layer, the evolution of PV above the boundary layer is determined by advection and diabatic effects. Considering axisymmetric, inviscid flow on an  $f$ -plane, and using radius  $r$ , height  $z$ , and time  $t$  as the independent variables, the PV equation takes the form

$$\frac{\partial P}{\partial t} + u \frac{\partial P}{\partial r} + w \frac{\partial P}{\partial z} = \frac{1}{\rho} \left[ -\frac{\partial v}{\partial z} \frac{\partial \theta}{\partial r} + \left( f + \frac{\partial(rv)}{r\partial r} \right) \frac{\partial \theta}{\partial z} \right], \quad (1)$$

<sup>6</sup>For a brief summary, see Haltiner and Martin (1957, pages 239–240).

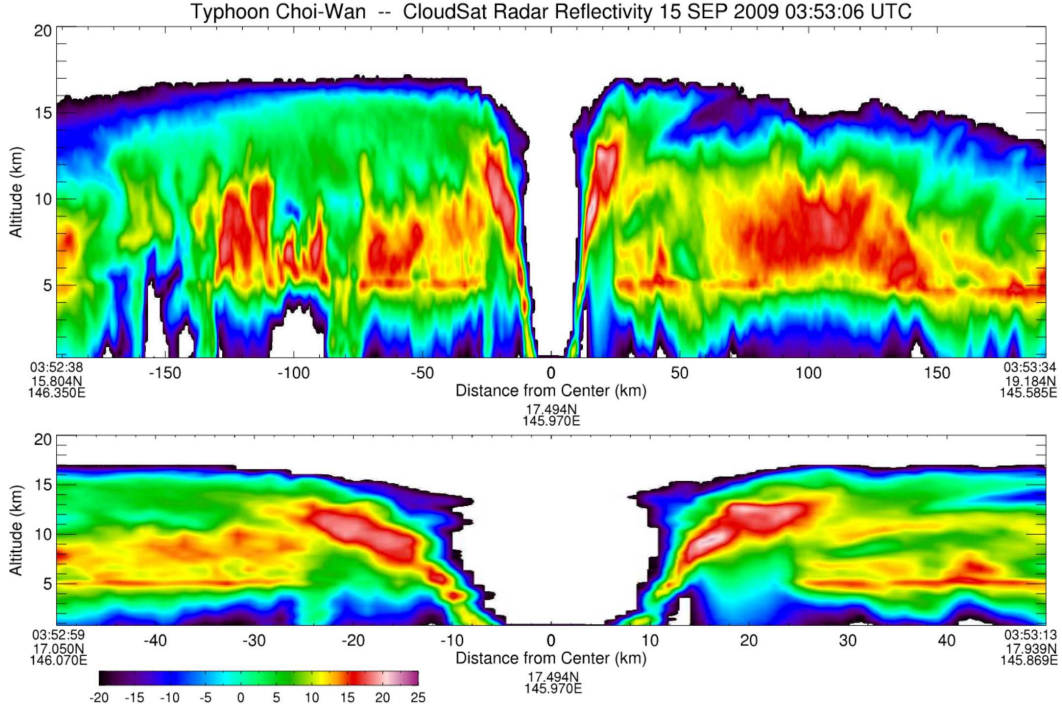


FIG. 1. At 0353 UTC on 15 September 2009, CloudSat’s 94 GHz Cloud Profiling Radar passed directly over Typhoon Choi-Wan. This figure shows a north-south vertical cross-section of radar reflectivity for the  $65 \text{ m s}^{-1}$  storm (north is to the right) when it was located approximately 450 km north of Guam. As is customary, in the top panel the horizontal scale is considerably compressed to exaggerate the vertical structure. In the bottom panel, only the region inside a radius of 50 km is shown (which excludes the secondary eyewall), but the aspect ratio is one-to-one, thus showing the sloping eyewall as would be seen by an observer on a research aircraft. This “stadium effect” is what Haurwitz referred to as the “funnel effect.” Reflectivity values less than -20 dBZ have been removed for clarity. This radar data is courtesy of the NASA CloudSat Project.

where  $u$  is the radial velocity,  $v$  the azimuthal velocity,  $w$  the vertical velocity,  $\rho$  the density,  $\dot{\theta}$  the diabatic heating, and where the potential vorticity is given by

$$P = \frac{1}{\rho} \left[ -\frac{\partial v}{\partial z} \frac{\partial \theta}{\partial r} + \left( f + \frac{\partial(rv)}{r \partial r} \right) \frac{\partial \theta}{\partial z} \right] = \frac{fR}{\rho r} \frac{\partial(R, \theta)}{\partial(r, z)}, \quad (2)$$

with the potential radius  $R$  defined in terms of the absolute angular momentum by  $\frac{1}{2}fR^2 = rv + \frac{1}{2}fr^2$ . We will now collapse the partial differential equation (1) into two simple ordinary differential equations, which can be solved analytically. To accomplish this simplification, first transform from the original independent variables  $(r, z, t)$  to the new independent variables  $(R, \theta, \tau)$ , where  $\tau = t$ , but  $\partial/\partial\tau$  means that  $R$  and  $\theta$  are fixed, while  $\partial/\partial t$  means that  $r$  and  $z$  are fixed. Then, the  $(r, z, t)$ -form of the material derivative is related the  $(R, \theta, \tau)$ -form by

$$\frac{\partial}{\partial t} + u \frac{\partial}{\partial r} + w \frac{\partial}{\partial z} = \frac{\partial}{\partial \tau} + \dot{R} \frac{\partial}{\partial R} + \dot{\theta} \frac{\partial}{\partial \theta}, \quad (3)$$

where  $\dot{R}$  is the rate that fluid particles are crossing  $R$ -surfaces. For inviscid axisymmetric flow, the absolute angular momentum is materially conserved, so that  $\dot{R} = 0$ , which simplifies the right-hand side of (3) and hence the left-hand side of (1). The right-hand side of (1) can also be simplified by writing it as

$$\frac{1}{\rho} \left[ -\frac{\partial v}{\partial z} \frac{\partial \dot{\theta}}{\partial r} + \left( f + \frac{\partial(rv)}{r \partial r} \right) \frac{\partial \dot{\theta}}{\partial z} \right] = \frac{fR}{\rho r} \frac{\partial(R, \dot{\theta})}{\partial(r, z)} = \frac{fR}{\rho r} \frac{\partial(R, \theta)}{\partial(r, z)} \frac{\partial(R, \dot{\theta})}{\partial(R, \theta)} = P \frac{\partial \dot{\theta}}{\partial \theta}, \quad (4)$$

where the second equality makes use of the Jacobian chain rule and the third equality makes use of (2). Then, using (3) and (4) in (1), the PV equation becomes

$$\frac{\partial P}{\partial \tau} + \dot{\theta} \frac{\partial P}{\partial \theta} = P \frac{\partial \dot{\theta}}{\partial \theta}. \quad (5)$$

The PV dynamics (5), which is equivalent to (1), can now be written in the characteristic form

$$\frac{d \ln P}{d \tau} = \frac{\partial \dot{\theta}}{\partial \theta} \quad \text{on} \quad \frac{d \theta}{d \tau} = \dot{\theta}, \quad (6)$$

where  $(d/d\tau) = (\partial/\partial\tau) + \dot{\theta}(\partial/\partial\theta)$  is the derivative along the characteristic. The reduction of the original equation (1) to the pair of ordinary differential equations (6) is a significant simplification, especially because these two ordinary differential equations can be solved sequentially. For a given diabatic heating  $\dot{\theta}$ , the first equation in (6) gives the variation of  $P$  along a characteristic, while the second equation gives the shape of that characteristic.

For the example considered here, we assume that  $\dot{\theta}$  is independent of  $\tau$  and has the separable form

$$\dot{\theta}(R, \theta) = \dot{\Theta}(R) \sin\left(\frac{\pi(\theta - \theta_B)}{\theta_T - \theta_B}\right), \quad (7)$$

where  $\dot{\Theta}(R)$  is a specified function, and where the bottom isentrope  $\theta_B$  and the top isentrope  $\theta_T$  are constants. In the following, we choose  $\theta_B = 300$  K and  $\theta_T = 360$  K, so that the maximum values of  $\dot{\theta}(R, \theta)$  occur on the  $\theta = 330$  K surface. For the mean tropical atmosphere, the  $\theta = 330$  K isentropic surface is very near the 425 hPa isobaric surface, which is a reasonable location for the maximum in  $\dot{\theta}$ . However, in the warm-core of an intense tropical cyclone the 330 K isentropic surface can bend considerably downward, making the assumption (7) less tenable. Thus, the example given here should be regarded as most applicable to the early phase in the formation of a PV tower.

Using (7) in the second equation of (6), we obtain

$$\frac{\left(\frac{\pi}{\theta_T - \theta_B}\right) d\theta}{\sin\left(\frac{\pi(\theta - \theta_B)}{\theta_T - \theta_B}\right)} = d\tau_c, \quad \text{where} \quad \tau_c = \frac{\pi \dot{\Theta}(R) \tau}{\theta_T - \theta_B}. \quad (8)$$

The dimensionless convective clock  $\tau_c(R)$  runs at different rates on different  $R$ -surfaces. In the eyewall, where  $\dot{\Theta}(R)$  is large, the  $\tau_c$ -clock advances quickly, while in the eye and the far-field, where  $\dot{\Theta}$  is small, the  $\tau_c$ -clock advances slowly. Note that, for a given  $R$ , the actual time  $\tau = (\theta_T - \theta_B)/\dot{\Theta}(R)$  corresponds to the dimensionless convective clock time  $\tau_c = \pi$  and can be considered as the tropospheric convective overturning time on that absolute angular momentum surface. Integration of (8) yields the characteristic equation

$$\theta(\vartheta, \tau_c) = \theta_B + \frac{2(\theta_T - \theta_B)}{\pi} \tan^{-1} \left[ e^{\tau_c} \tan\left(\frac{\pi(\vartheta - \theta_B)}{2(\theta_T - \theta_B)}\right) \right], \quad (9)$$

where  $\vartheta$  is the label of the characteristic, i.e., the initial potential temperature of the characteristic. To confirm that (9) satisfies the initial condition, note that the  $e^{\tau_c}$  factor becomes unity when  $\tau_c = 0$  and that the inverse tangent and tangent operations then cancel, so that (9) reduces to  $\theta = \vartheta$  when  $\tau_c = 0$ . The red curves in Fig. 2 are the characteristics  $\theta(\vartheta, \tau_c)$  given by (9), with  $\vartheta$  starting at  $\vartheta = 301$  K and then incremented by 1 K up to  $\vartheta = 359$  K. Note that these characteristics bend upward most rapidly at  $\theta = 330$  K, where the value of  $\dot{\theta}$  is largest. The form (9) is useful for plotting the characteristics because, for a given  $\vartheta$ , it allows for explicit calculation of  $\theta$  as a function of  $\tau_c$ . As we shall see shortly, it is also useful to rearrange (9) into the form

$$\vartheta(\theta, \tau_c) = \theta_B + \frac{2(\theta_T - \theta_B)}{\pi} \tan^{-1} \left[ e^{-\tau_c} \tan\left(\frac{\pi(\theta - \theta_B)}{2(\theta_T - \theta_B)}\right) \right], \quad (10)$$

which can be regarded as giving the initial potential temperature of the characteristic that goes through the point  $(\theta, \tau_c)$ .

We now turn our attention to the solution of the first ordinary differential equation in (6). With the previous assumption (7) that  $\dot{\theta}$  depends only on  $(R, \theta)$ , and now assuming that the initial potential vorticity is the constant  $P_0$ , the solution of the first equation in (6) is

$$P(\theta, \tau_c) = P_0 \left( \frac{\dot{\theta}(R, \theta)}{\dot{\theta}(R, \vartheta(\theta, \tau_c))} \right). \quad (11)$$

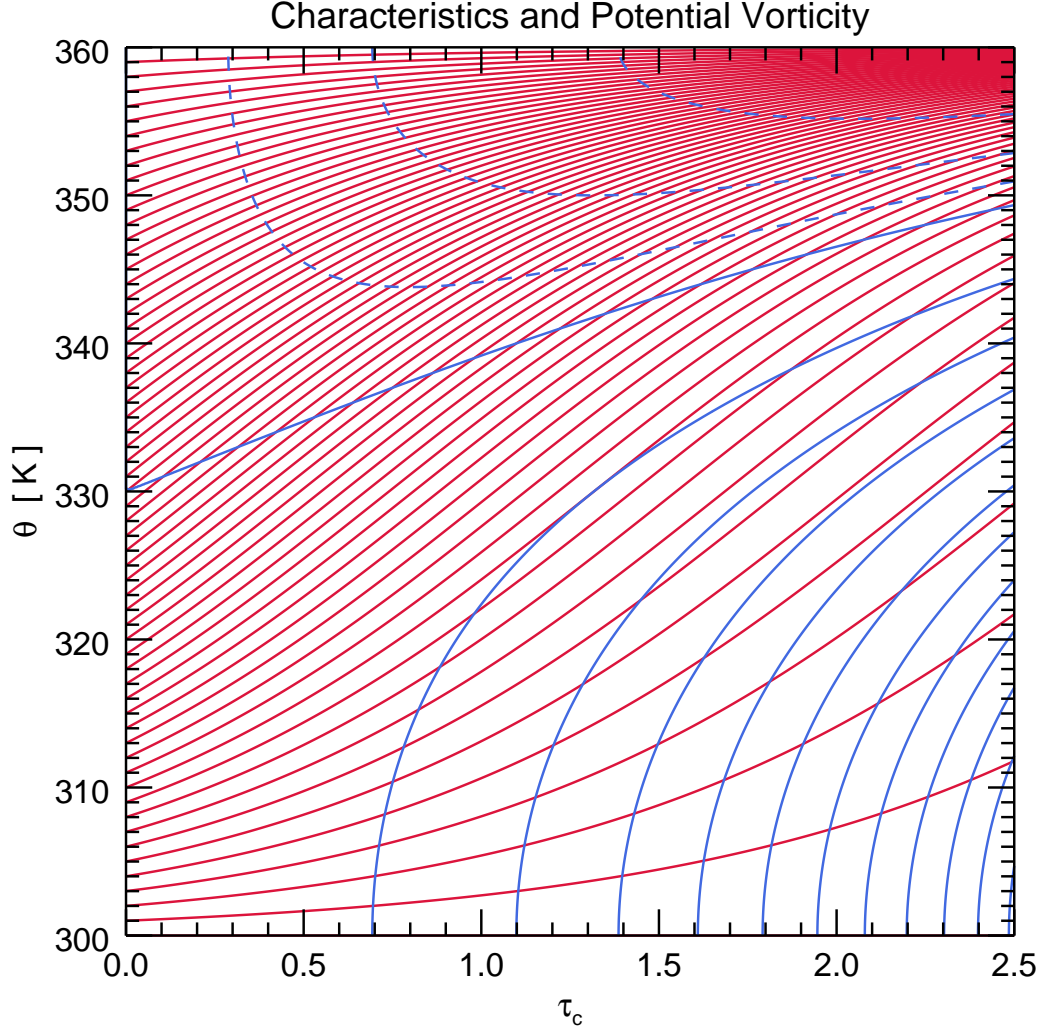


FIG. 2. The red curves are the characteristics  $\theta(\vartheta, \tau_c)$  determined from (9), with  $\vartheta$  denoting the characteristic label (i.e., the initial value of the potential temperature) and  $\tau_c$  denoting the dimensionless convective clock defined in the second entry of (8). The blue curves are isolines of  $P(\theta, \tau_c)/P_0$ , as determined from (12) and (13). The blue isoline starting at 330 K corresponds to  $P(\theta, \tau_c)/P_0 = 1$ , with the other solid isolines corresponding to  $P(\theta, \tau_c)/P_0 = 2, 3, \dots, 11$  and the dashed lines corresponding to  $P(\theta, \tau_c)/P_0 = 1/2, 1/4, 1/8$ .

One way to confirm that (11) is the required solution is to simply take  $(d/d\tau)$  of the natural logarithm of (11). Another way is to note that, under our assumption that  $\hat{\theta}$  is independent of  $\tau$ , the quantity  $\hat{\theta}/P$  becomes a Riemann invariant, i.e.,  $(d/d\tau)(\hat{\theta}/P) = 0$ , from which (11) immediately follows. Using (7) and (10) in (11), we obtain the final solution

$$P(\theta, \tau_c) = P_0 \left( \frac{\sin\left(\frac{\pi(\theta - \theta_B)}{\theta_T - \theta_B}\right)}{\sin\left\{2 \tan^{-1}\left[e^{-\tau_c} \tan\left(\frac{\pi(\theta - \theta_B)}{2(\theta_T - \theta_B)}\right)\right]\right\}} \right). \quad (12)$$

Although the right-hand side of (13) is indeterminate at the boundaries  $\theta = \theta_B, \theta_T$ , use of L'Hospital's rule yields

$$P(\theta, \tau_c) = P_0 \begin{cases} e^{-\tau_c} & \text{if } \theta = \theta_T \\ e^{\tau_c} & \text{if } \theta = \theta_B. \end{cases} \quad (13)$$

Isolines of the dimensionless potential vorticity  $P(\theta, \tau_c)/P_0$  are shown by the blue curves in Fig. 2. The largest value of PV attained on any of the 59 characteristic curves (red) occurs at  $\tau_c = 2.5$  along the characteristic originating from

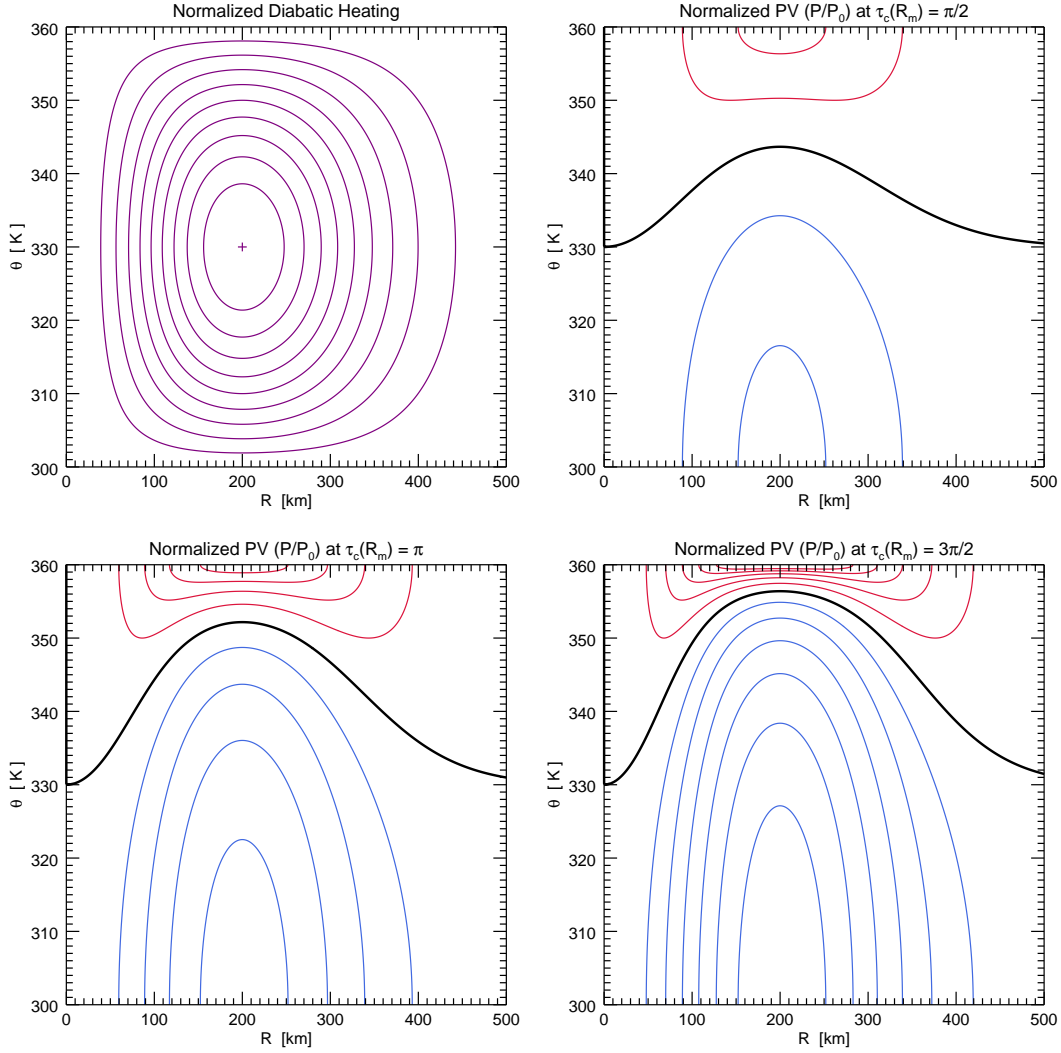


FIG. 3. The upper left panel shows isolines of  $\dot{\theta}(R, \theta)/\dot{\Theta}_m$ . The remaining three panels show isolines of  $P(R, \theta, \tau_c)/P_0$ , as determined from (12)–(14), for  $R_m = 200$  km and for the three times corresponding to  $\tau_c(R_m) = \pi/2, \pi, 3\pi/2$ .

$\theta = 301$  K. This characteristic remains close to the surface where the  $(\partial \dot{\theta}/\partial \theta)$ -term in (5) is large, with the result that  $P$  acquires the value  $11 P_0$  at  $\tau_c = 2.5$ . In the region  $300 \leq \theta \leq 330$  K both the  $\dot{\theta}(\partial P/\partial \theta)$  and the  $P(\partial \dot{\theta}/\partial \theta)$  terms in (3) contribute to positive  $(\partial P/\partial \tau)$ . In the region  $330 \leq \theta \leq 360$  K the  $P(\partial \dot{\theta}/\partial \theta)$ -term makes a negative contribution to  $(\partial P/\partial \tau)$ , but  $(\partial P/\partial \tau)$  remains positive because of the  $\dot{\theta}(\partial P/\partial \theta)$ -term. The net effect is that a tower of high PV grows into the upper troposphere.

To get a better appreciation of the formation of a PV tower, and in particular the formation of a hollow PV tower, consider the example  $\dot{\Theta}(R) = \dot{\Theta}_m (R/R_m)^2 \exp[1 - (R/R_m)^2]$ , where  $R_m$  is the potential radius where  $\dot{\Theta}(R)$  is a maximum and  $\dot{\Theta}_m$  is the value of this maximum. Using this  $\dot{\Theta}(R)$  in the second entry of (8), we obtain

$$\tau_c(R) = \tau_c(R_m) \left( \frac{R}{R_m} \right)^2 \exp \left[ 1 - \left( \frac{R}{R_m} \right)^2 \right], \quad \text{where} \quad \tau_c(R_m) = \frac{\pi \dot{\Theta}_m \tau}{\theta_\tau - \theta_b}. \quad (14)$$

Using (14) in (12), we can now produce  $(R, \theta)$ -cross-sections of PV at different times. Figure 3 shows isolines of PV in  $(R, \theta)$ -space for the choice  $R_m = 200$  km and for the three times  $\tau_c(R_m) = \pi/2, \pi, 3\pi/2$ . Note that a hollow tower of PV is produced.<sup>7</sup>

It is a difficult task to sample a hurricane's wind and mass fields in sufficient detail to produce PV maps and PV cross-sections. However, using dropsondes and airborne Doppler radar, this has recently been accomplished by

<sup>7</sup>For additional discussion, see Schubert and Alworth (1987) and Möller and Smith (1994).

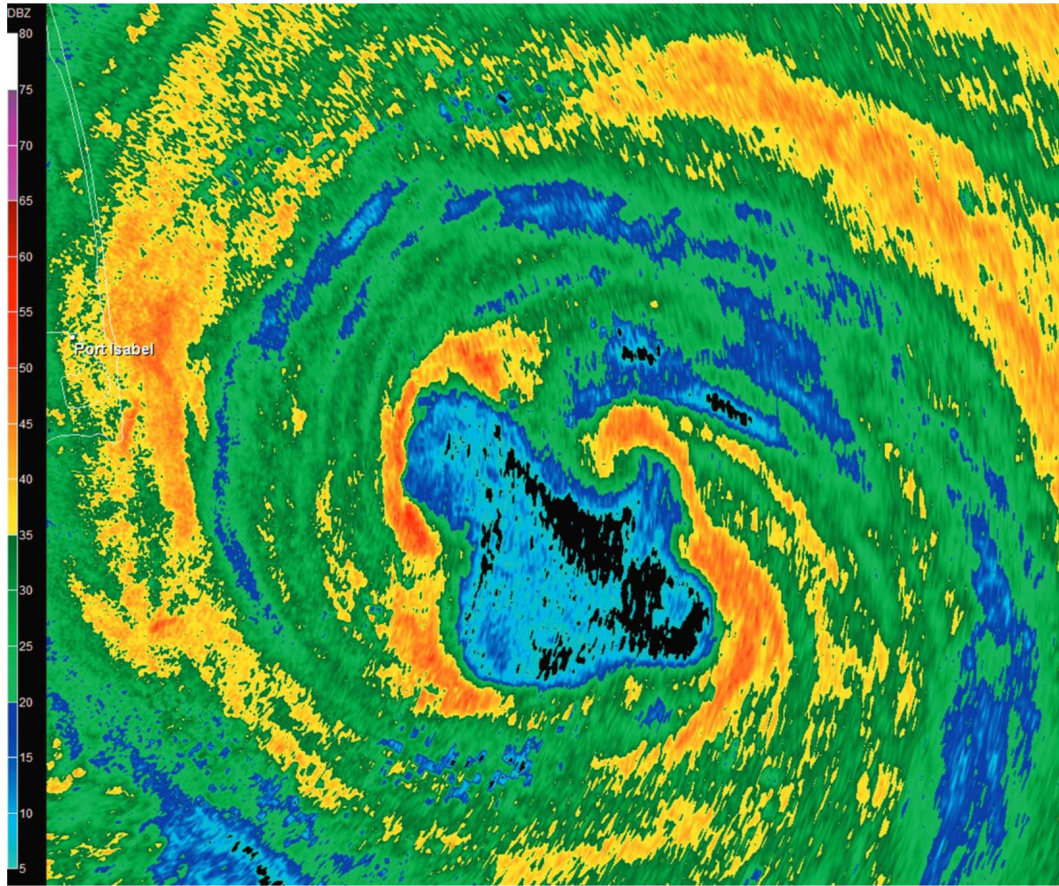


FIG. 4. Base reflectivity (dBZ color scale on the left) from the Brownsville, Texas, National Weather Service radar at 1052 UTC on 23 July 2008. At this time, Hurricane Dolly was approaching the coast, and asymmetries, including eye mesovortices and straight line segments, were observed in the inner core. From Hendricks et al. (2009).

Bell et al. (2017) for Hurricane Patricia (2015), a storm that rewrote the tropical cyclone record books (Rogers et al. 2017), including the record for the highest surface winds measured by aircraft ( $94 \text{ m s}^{-1}$ ), the highest flight-level winds measured by aircraft ( $99 \text{ m s}^{-1}$ ), and the most rapid intensification rate ( $54 \text{ m s}^{-1}$  in 24 hours). One of Bell et al.'s PV cross-sections can be seen in the slide version of this paper. It shows a very compact hollow tower of PV, with a maximum value of approximately 250 PV units.

### 3. Instability of PV rings

Figure 4 is a radar image of Hurricane Dolly (2008) as it approached the south Texas coast. The eye is characterized by the low reflectivity blue region and the eyewall by the surrounding red region. At this time, the hurricane was estimated to have maximum winds of  $41 \text{ m s}^{-1}$  and a central surface pressure of 976 hPa. The wavenumber-4 pattern in the eyewall is believed to be the result of the barotropic instability of a thin PV ring. During the past two decades, the instability of PV rings has been studied using a hierarchy of models. This hierarchy can be conveniently divided into the four levels listed below, starting with the simplest nondivergent barotropic models and ending with the most complicated nonhydrostatic, full-physics models.

#### *a. Nondivergent barotropic models*

The simplest analysis of PV rings involves the eigenvalue-eigenfunction calculation of the exponential instability of idealized basic states and then the numerical integration of such small amplitude initial unstable flows into their finite amplitude, nonlinear regime (Schubert et al. 1999; Kossin and Schubert 2001; Hendricks et al. 2009; Menelaou et al. 2013a). These studies of the life cycles of unforced, hurricane-like vorticity rings have been extended



to the forced case by Rozoff et al. (2009), who used a nondivergent barotropic model to study vortex intensification due to ring forcing. The results showed that a smooth intensification can be interrupted in two ways. It can be either slowed by a “vorticity mixing intensification brake” or enhanced by efficient transport of vorticity from the eyewall generation region to the eye. Thus, there can be a dual nature of potential vorticity mixing. In addition to exponential instability, it is possible for hurricane-like vortices to exhibit algebraic instability, which can occur when the vortex has a maximum in the basic-state angular velocity other than at the center of circulation. The dynamics of this algebraic instability has been studied in the context of the near-core dynamics of hurricanes by Nolan and Montgomery (2000).

#### *b. Divergent barotropic models*

The barotropic instability of hurricane-scale annular PV rings was first explored by Guinn (1992) using a nonlinear shallow water model that was solved by a normal mode spectral method, thus allowing the total flow to be partitioned into its rotational and gravitational components. As a generalization of the forced nondivergent barotropic model studies discussed above, Hendricks et al. (2014) used a forced shallow water model to understand the role of diabatic and frictional effects in the generation, maintenance, and breakdown of the hurricane eyewall PV ring. Diabatic heating was parameterized as an annular mass sink of variable width and magnitude. The mass sink produced a strengthening and thinning PV ring, with dynamic instability occurring if the ring became thin enough. The onset of instability was marked by drops in both the maximum velocity and the minimum central pressure. The most recent research along these lines is that of Lahaye and Zeitlin (2016), who have formulated a unique moist convective shallow water model.

#### *c. Three-dimensional hydrostatic models*

To better understand the vertical structure of PV mixing, Hendricks and Schubert (2010) used an isentropic coordinate model to study the adiabatic rearrangement of hollow PV towers. The model does not include diabatic effects, but it shows that in physically relevant cases the instability is most vigorous in the lower troposphere.

#### *d. Three-dimensional nonhydrostatic, full-physics models*

Nolan and Montgomery (2002) studied the dry dynamics of linearized perturbations to hurricane-like vortices. The perturbations were allowed to be fully three-dimensional and nonhydrostatic, but for their hurricane-like basic states the instabilities were found to be close analogs of those found in barotropic models. The appearance of unstable PV rings in nonlinear, full-physics models has been documented by several modeling groups, including Zhang et al. (2002), Yau et al. (2004), Kwon and Frank (2005), Mashiko (2005), Wang (2008, 2009), Judt and Chen (2010), Menelaou et al. (2013b), Naylor and Schechter (2014), and Wu et al. (2016). The Naylor and Schechter simulations use the CM1 model with 250 m horizontal resolution, which is more than ten times finer than the 3 km resolution often used in WRF simulations. An interesting conclusion of Naylor and Schechter is that the initial moist model wave growth leading to polygonal eyewalls and mesovortices closely resembles that found in a dry non-convective vortex with the same tangential flow. The agreement between the moist and dry models is at least partly due to the fact that the bulk of the cloudy eyewall updraft is outside the vorticity ring in which the instability occurs.

In addition to the above modeling research, there are many observational studies that relate to PV rings. These go back to the first reports of polygonal eyewalls by Lewis and Hawkins (1982) and Muramatsu (1986). Later, using aircraft data, Kossin and Eastin (2001) found that the kinematic and thermodynamic distributions within the eye and eyewall of strong hurricanes evolved between two distinct regimes. In the first regime, angular velocity was greatest within the eyewall and relatively depressed within the eye. In the second regime, radial profiles of angular velocity were nearly monotonic with maxima found at the eye center. The evolution of these kinematic distributions was often marked by a transition from the first regime to the second with the transition possibly occurring in less than one hour. Landfalling hurricanes are often well-observed by coastal radars and can provide valuable insights, as in the Hurricane Dolly (2008) study of Hendricks et al. (2012) and the Hurricane Ike (2008) study of Wingo and Knupp (2016). A case that is under active study is the Hurricane Patricia case (Rogers et al. 2017). Finally, we note that there are some very interesting laboratory experiments relevant to the instability of PV rings. These have been performed using water as the working fluid (Montgomery et al. 2002) or using a pure electron plasma in a cylindrical trap (Peurrung and Fajans 1993; Fine et al. 1995).

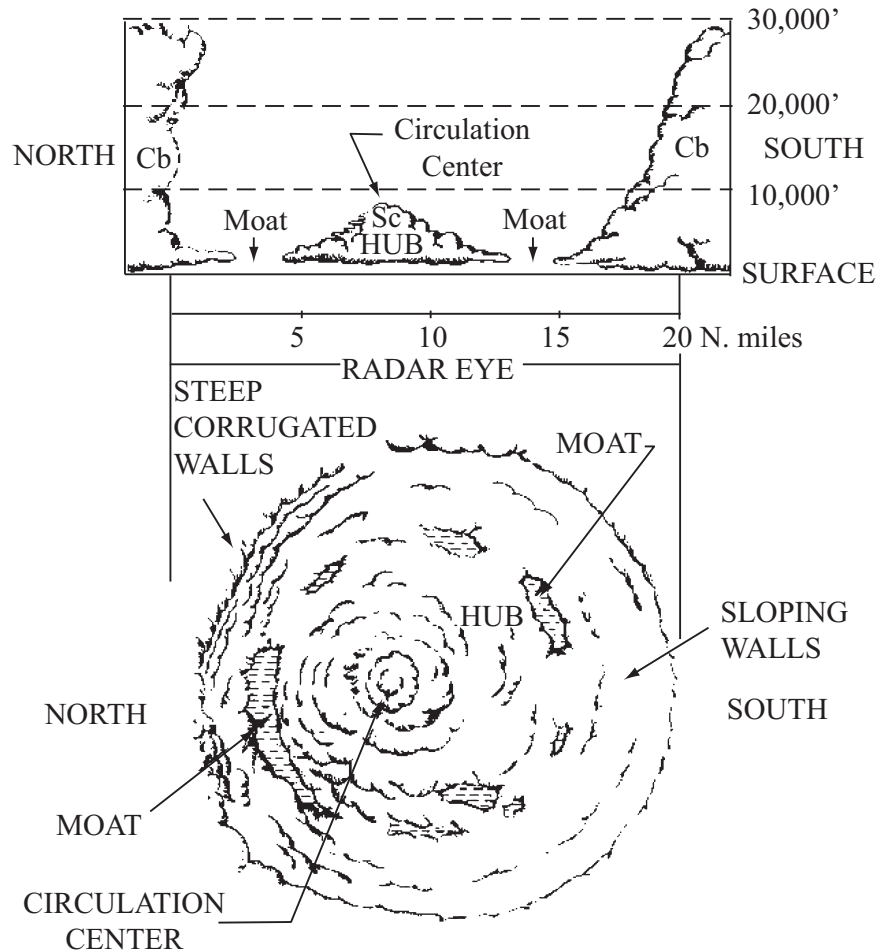


FIG. 5. Schematic diagram of the eye of Hurricane Edna, 9–10 September 1954, as adapted from Simpson and Starrett (1955).

#### 4. Subsidence in the eye: hub clouds, eye moats, and warm rings

The concept of hub clouds and eye moats comes from observations made by Simpson and Starrett (1955). Figure 5 is adapted from their schematic diagram of Hurricane Edna (9–10 September 1954). Of particular interest is the hub cloud near the circulation center and the clear moat at the edge of the eye. In later years, intense storms like Edna have been found to also possess a warm-ring thermal structure in the lower troposphere. A good example is Hurricane Isabel on 13 September 2003, when it had tangential winds in excess of  $70 \text{ m s}^{-1}$ . Figure 6 shows NOAA WP-3D aircraft data for this storm.<sup>8</sup> The two panels show tangential wind (black lines), temperature (red lines), and dewpoint temperature (blue lines) for a 2.1 km altitude radial leg (lower panel) and a 3.7 km altitude radial leg (upper panel). A warm-ring thermal structure is seen at both altitudes, with the ring approximately  $4.2^\circ\text{C}$  warmer than the vortex center at 3.7 km and  $5.0^\circ\text{C}$  warmer than the vortex center at 2.1 km. As can be seen from the dewpoint depressions, the warm-ring region near 25 km radius is associated with dry, subsiding air at the outer edge of the eye. Enhanced subsidence at the outer edge of the eye tends to produce an eye-moat. The photograph shown here as Fig. 7 was taken from the WP-3D aircraft near the edge of the eye, looking towards the hub cloud at the center of the eye. The top of the hub cloud is near 3 km altitude, so the radial leg in the upper panel of Fig. 6 is just above the top of the hub cloud, while the radial leg in the lower panel is just below the top of the hub cloud, as is evident in the dewpoint depressions.

<sup>8</sup>For comprehensive discussions of Hurricane Isabel, see Montgomery et al. (2006), Aberson et al. (2006), Schubert et al. (2007), Bell and Montgomery (2008), and Nolan et al. (2009b,a). The eye-moat and mesovortex structure of Hurricane Isabel on the previous day (12 September) is discussed by Kossin and Schubert (2004) and Rozoff et al. (2006).

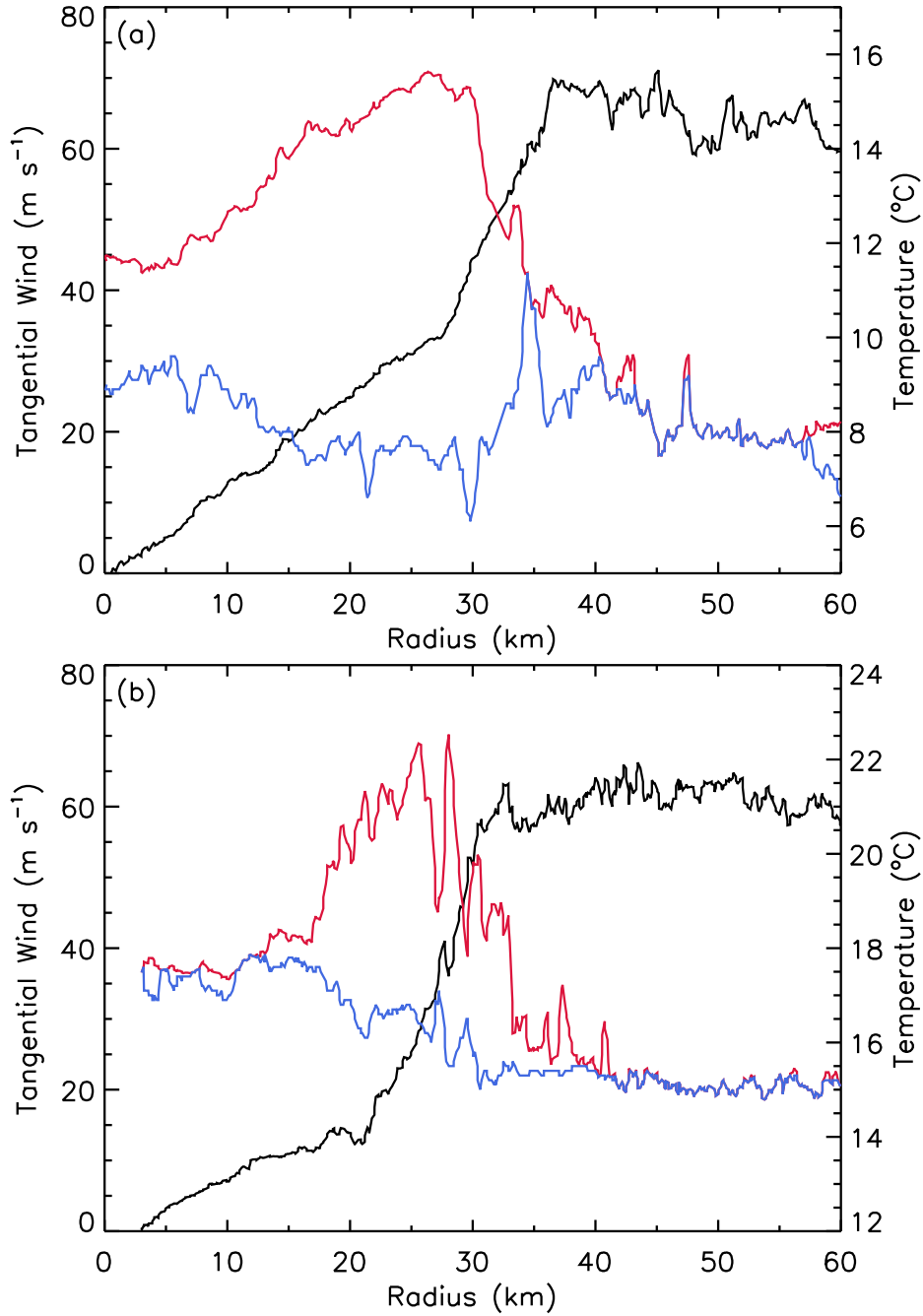


FIG. 6. Radial profiles of NOAA WP-3D aircraft data for Hurricane Isabel on 13 September 2003. The upper panel is for the  $z = 3.7$  km flight leg (1948 to 1956 UTC) and the lower panel for the  $z = 2.1$  km flight leg (1922 to 1931 UTC). Black curves are for tangential wind, red curves for temperature, and blue curves for dewpoint temperature. Adapted from Schubert et al. (2007).

For simplicity, the analysis in this section considers an axisymmetric, balanced flow in the inviscid fluid that lies above the frictional boundary layer. To simplify the primitive equation model to a balanced vortex model, we assume that the azimuthal flow remains in a gradient balanced state, i.e., we discard the radial equation of motion and replace it with the gradient balance condition given below as the first entry in (15). A sufficient condition for the validity of this assumption is that the diabatic forcing effects have slow enough time scales that significant, azimuthal mean



FIG. 7. Photograph of the eye of Hurricane Isabel on 13 September 2003. The 3 km tall hub cloud at the center of the eye is surrounded by a moat of clear air or shallow stratocumulus. Beyond the hub cloud and on the opposite side of the eye (at a distance of  $\sim 60$  km) lies eyewall convection extending up to 12–14 km. Since the first internal mode Rossby length in the eye of Isabel at this time is approximately 13 km, the eye diameter is approximately 5 Rossby lengths, allowing for the rare opportunity to view balanced dynamical structure over several Rossby lengths in a single photograph. Photo courtesy of Sim Aberson.

inertia-gravity waves are not excited. We shall describe this inviscid flow using the log-pressure vertical coordinate  $z = H \ln(p_0/p)$ , where  $H = R_d T_0/g$  is the constant scale height,  $p_0$  and  $T_0$  are constant reference values of pressure and temperature,  $R_d$  is the gas constant for dry air, and  $g$  is the acceleration of gravity. Under the balance condition, the governing equations are

$$\begin{aligned} \left(f + \frac{v}{r}\right)v = \frac{\partial \phi}{\partial r}, \quad \frac{\partial v}{\partial t} + w \frac{\partial v}{\partial z} + \left(f + \frac{\partial(rv)}{r \partial r}\right)u = 0, \quad \frac{\partial \phi}{\partial z} = \frac{g}{T_0} T, \\ \frac{\partial(e^{-z/H} r u)}{r \partial r} + \frac{\partial(e^{-z/H} w)}{\partial z} = 0, \quad \frac{\partial T}{\partial t} + u \frac{\partial T}{\partial r} + w \left(\frac{\partial T}{\partial z} + \frac{RT}{c_p H}\right) = \frac{Q}{c_p}, \end{aligned} \quad (15)$$

where  $f$  is the constant Coriolis parameter,  $\phi$  the geopotential,  $u$  the radial velocity component,  $v$  the azimuthal velocity component,  $w$  the log-pressure vertical velocity, and  $Q$  the diabatic heating.

The thermal wind equation is derived by eliminating  $\phi$  between the hydrostatic equation and the gradient wind equation. Then, taking  $\partial/\partial t$  of this thermal wind equation, we obtain

$$\frac{\partial}{\partial z} \left[ \left(f + \frac{2v}{r}\right) \frac{\partial v}{\partial t} \right] = \frac{g}{T_0} \frac{\partial}{\partial r} \left( \frac{\partial T}{\partial t} \right), \quad (16)$$

which is the constraint that must be satisfied by the local time derivatives of the azimuthal wind field and the temperature field. Using the mass conservation principle, we define a streamfunction  $\psi$  such that

$$e^{-z/H} u = -\frac{\partial \psi}{\partial z}, \quad e^{-z/H} w = \frac{\partial(r\psi)}{r \partial r}. \quad (17)$$

Using (17) in the second and fifth entries of (15), we obtain

$$-\left(f + \frac{2v}{r}\right) \frac{\partial v}{\partial t} + B \frac{\partial(r\psi)}{r \partial r} + C \frac{\partial \psi}{\partial z} = 0, \quad \frac{g}{T_0} \frac{\partial T}{\partial t} + A \frac{\partial(r\psi)}{r \partial r} + B \frac{\partial \psi}{\partial z} = \frac{g}{c_p T_0} Q, \quad (18)$$

where the static stability  $A$ , the baroclinicity  $B$ , and the inertial stability  $C$  are given by

$$e^{-z/H} A = \frac{g}{T_0} \left( \frac{\partial T}{\partial z} + \frac{R_d T}{c_p H} \right), \quad e^{-z/H} B = - \left( f + \frac{2v}{r} \right) \frac{\partial v}{\partial z} = - \frac{g}{T_0} \frac{\partial T}{\partial r}, \quad (19)$$

$$e^{-z/H} C = \left( f + \frac{2v}{r} \right) \left( f + \frac{\partial(rv)}{r \partial r} \right) \equiv \hat{f}^2.$$

Adding  $\partial/\partial r$  of the second entry in (18) to  $\partial/\partial z$  of the first entry, we obtain the transverse circulation equation

$$\frac{\partial}{\partial r} \left( A \frac{\partial(r\psi)}{r \partial r} + B \frac{\partial \psi}{\partial z} \right) + \frac{\partial}{\partial z} \left( B \frac{\partial(r\psi)}{r \partial r} + C \frac{\partial \psi}{\partial z} \right) = \frac{g}{c_p T_0} \frac{\partial Q}{\partial r}. \quad (20)$$

Note that  $AC - B^2 = (g/T_0)e^{(1-\kappa)z/H} (f + 2v/r)P$ , where

$$P = e^{z/H} \left[ - \frac{\partial v}{\partial z} \frac{\partial \theta}{\partial r} + \left( f + \frac{\partial(rv)}{r \partial r} \right) \frac{\partial \theta}{\partial z} \right] \quad (21)$$

is the potential vorticity. The partial differential equation (20) is elliptic if  $(f + 2v/r)P > 0$ .

In real tropical cyclones, the coefficients  $A$ ,  $B$ , and  $C$  can vary in complicated ways, making analytical solution of (20) impossible. However, we can understand several aspects of the transverse circulation by solution of a simplified version of (20). In this simplified version we assume  $B = 0$  and  $A = e^{z/H} N^2$ , where  $N$  is a constant. Under these assumptions, (20) simplifies to

$$N^2 \frac{\partial}{\partial r} \left( \frac{\partial(r\psi)}{r \partial r} \right) + \hat{f}^2 \frac{\partial}{\partial z} \left( e^{z/H} \frac{\partial \psi}{\partial z} \right) = \frac{g e^{-z/H}}{c_p T_0} \frac{\partial Q}{\partial r}. \quad (22)$$

It is important to note that the assumption  $B = 0$  precludes modeling the ‘‘stadium effect’’ that was seen in Fig. 1. Assuming the diabatic heating  $Q$ , the streamfunction  $\psi$ , and the vertical velocity  $w$  have the separable forms

$$Q(r, z) = \hat{Q}(r) e^{z/2H} \sin\left(\frac{\pi z}{z_T}\right), \quad \psi(r, z) = \hat{\psi}(r) e^{-z/2H} \sin\left(\frac{\pi z}{z_T}\right), \quad w(r, z) = \hat{w}(r) e^{z/2H} \sin\left(\frac{\pi z}{z_T}\right), \quad (23)$$

the partial differential equation (22) reduces to the ordinary differential equation

$$r^2 \frac{d^2 \hat{\psi}}{dr^2} + r \frac{d \hat{\psi}}{dr} - \left( \frac{r^2}{\ell^2} + 1 \right) \hat{\psi} = \frac{g r^2}{c_p T_0 N^2} \frac{d \hat{Q}}{dr}, \quad (24)$$

where

$$\hat{w} = \frac{d(r \hat{\psi})}{r dr} \quad \text{and} \quad \ell = \frac{N}{\hat{f}} \left( \frac{\pi^2}{z_T^2} + \frac{1}{4H^2} \right)^{-1/2}. \quad (25)$$

Since  $\hat{f}$  is a function of radius,  $\ell$  is also a function of radius and can be interpreted as the local Rossby length.

To solve (24), we need to know the horizontal structure of the forcing  $\hat{Q}(r)$  and the horizontal structure of the local Rossby length  $\ell(r)$ , and we need to enforce the boundary conditions  $\hat{\psi}(0) = 0$  and  $r \hat{\psi}(r) \rightarrow 0$  as  $r \rightarrow \infty$ . However, to understand the distribution of subsidence in the eye, all we need to know is that, in the eye, equation (24) becomes homogeneous and, to a good approximation,  $\ell(r)$  takes on a constant ‘‘core value’’  $\ell_c$ . Thus, (24) becomes

$$r^2 \frac{d^2 \hat{\psi}}{dr^2} + r \frac{d \hat{\psi}}{dr} - \left( \frac{r^2}{\ell_c^2} + 1 \right) \hat{\psi} = 0 \quad \text{for} \quad 0 \leq r < r_m, \quad (26)$$

where  $r_m$  is the radius of maximum tangential wind, which in the context of the present discussion can also be interpreted as the radius of the eye. The solution of (26) is a linear combination of the order one modified Bessel functions  $I_1(r/\ell_c)$  and  $K_1(r/\ell_c)$ . Because  $K_1(r/\ell_c)$  is singular at  $r = 0$ , only the  $I_1(r/\ell_c)$  solution is accepted in the region  $0 \leq r < r_m$ . Since  $d[r I_1(r/\ell_c)]/dr = (r/\ell_c) I_0(r/\ell_c)$ , the horizontal distribution of eye subsidence  $\hat{w}(r)$  is proportional to the order zero modified Bessel function  $I_0(r/\ell_c)$ . Both  $I_0(r/\ell_c)$  and  $I_1(r/\ell_c)$  are plotted in Fig. 8. Since the transverse circulation problem is elliptic, the coefficient multiplying the  $I_0(r/\ell_c)$  function depends on both the boundary conditions and the diabatic forcing over the entire domain. However, for the purposes of the present discussion, we are interested only in the relative spatial variation of the subsidence, not in its magnitude. Thus, we

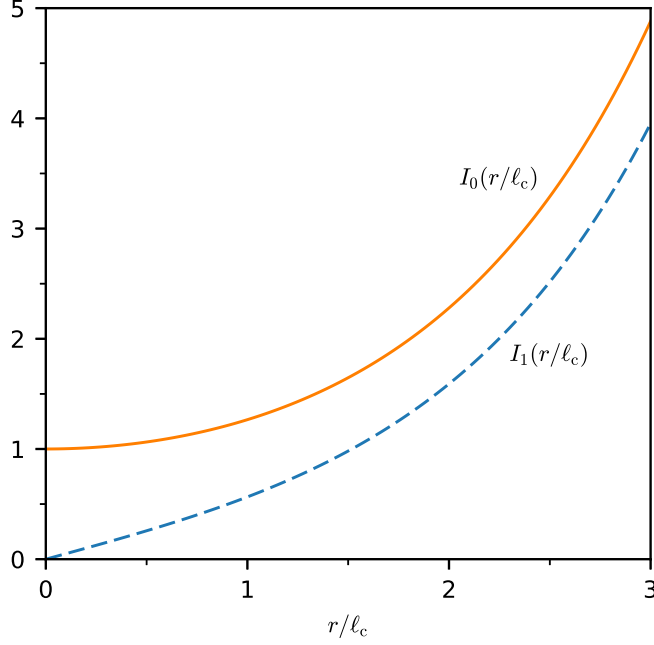


FIG. 8. The order-one modified Bessel function  $I_1(r/\ell_c)$ , from which the streamfunction  $\hat{\psi}$  is constructed, and the order-zero modified Bessel function  $I_0(r/\ell_c)$ , from which the vertical motion  $\hat{w}$  is constructed.

can simply normalize the eye solution through the use of  $\bar{w}$ , the area-averaged subsidence in the eye, defined by  $\bar{w} = (2/r_m^2) \int_0^{r_m} \hat{w}(r) r dr$ . Using this normalization, the eye solution can be expressed as

$$\frac{\hat{w}(r)}{|\bar{w}|} = -\frac{(r_m/\ell_c) I_0(r/\ell_c)}{2I_1(r_m/\ell_c)} \quad \text{for } 0 \leq r < r_m. \quad (27)$$

The consistency of (27) with the definition of  $\bar{w}$  can easily be checked by taking the area integral of (27) and using the integral relation  $\int_0^x I_0(x') x' dx' = x I_1(x)$ . Three useful special cases of (27) are

$$\frac{\hat{w}(r)}{|\bar{w}|} = \begin{cases} -0.3794 I_0(3r/r_m) & \text{if } r_m = 3\ell_c \ (v_m = 75) \\ -0.6287 I_0(2r/r_m) & \text{if } r_m = 2\ell_c \ (v_m = 50) \\ -0.8847 I_0(r/r_m) & \text{if } r_m = \ell_c \ (v_m = 25). \end{cases} \quad (28)$$

Plots of (28) are shown in Fig. 9. The three colored curves have the same area-averaged subsidence over the eye-region. The  $r_m = 3\ell_c$  case (green curve) has the largest spatial variation of eye subsidence, with a subsidence rate at the outer edge of the eye nearly five times the value at the center. Slow variation of the intensity of eyewall convection moves these eye-subsidence profiles up-and-down but does not alter their shape.

The estimates of  $v_m$  given in (28) are determined as follows. As a first approximation to the inner core radial structure of the azimuthal wind, we assume that  $v(r)$  increases linearly with  $r$  to the maximum value  $v_m$  at the radius  $r_m$ . Then,  $\hat{f}$  simplifies to  $f + 2v_m/r_m$  in the inner core, so that, according to (25), the constant Rossby length in the core is given by

$$\ell_c = \left( \frac{f}{f + 2v_m/r_m} \right) \ell_0, \quad \text{where} \quad \ell_0 = \frac{N}{f} \left( \frac{\pi^2}{z_T^2} + \frac{1}{4H^2} \right)^{-1/2} = \frac{c}{f} \approx \frac{50 \text{ ms}^{-1}}{5 \times 10^{-5} \text{ s}^{-1}} \approx 1000 \text{ km}, \quad (29)$$

where  $c$  is the gravity wave speed of the first internal mode. Using (29), the “dimensionless dynamical eye radius”  $r_m/\ell_c$  can be written as

$$\frac{r_m}{\ell_c} = \frac{(f + 2v_m/r_m) r_m}{c}. \quad (30)$$

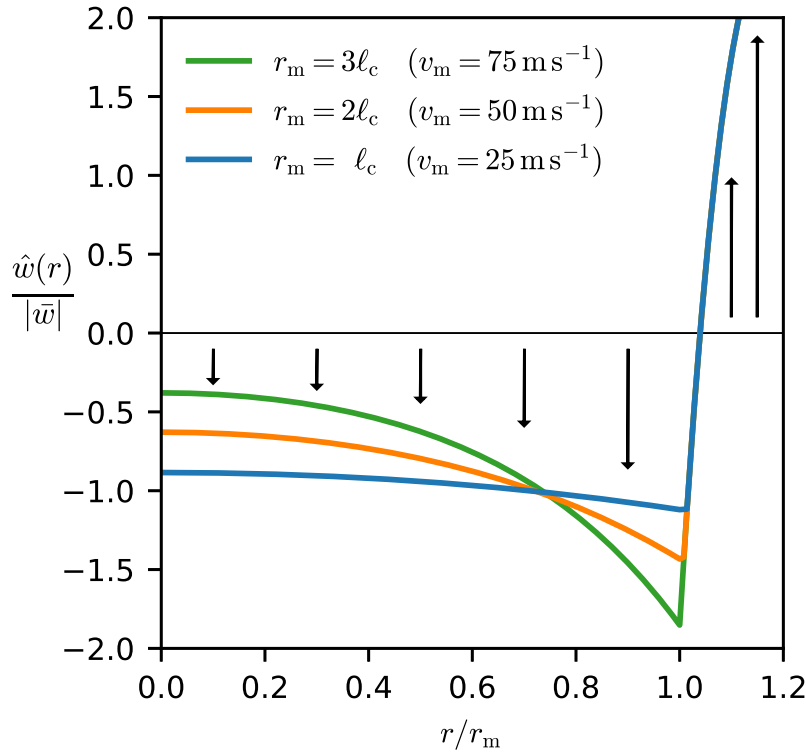


FIG. 9. Normalized vertical motion  $\hat{w}(r)/|\bar{w}|$  as a function of radius, computed from (28) for the eye region  $0 \leq r/r_m < 1$  and simply shown schematically for the eyewall updraft region. The three colored curves have the same area-averaged subsidence over the eye-region. The  $r_m = 3\ell_c$  case (green curve) has the largest spatial variation of eye subsidence, with a subsidence rate at the outer edge of the eye nearly five times the value at the center.

The orange curves in Fig. 10 are isolines of the core Rossby length  $\ell_c$  in the  $(r_m, v_m)$ -plane. These isolines have been computed from (29). The blue curves in Fig. 10 are isolines of  $r_m/\ell_c$ , i.e., the actual eye radius  $r_m$  measured in units of the core Rossby length  $\ell_c$ . The blue curves have been computed from (30). Note that the dimensionless dynamical eye radius  $r_m/\ell_c$  is essentially independent of the actual eye radius  $r_m$  and depends only on  $v_m$ . In other words, to a first approximation, a set of tropical cyclones with the same values of  $v_m$  but widely varying actual eye sizes, all have essentially the same dynamical eye size and hence the same tendency to produce a warm-ring thermal structure. The weak dependence of  $r_m/\ell_c$  on  $r_m$  can be understood by noting that, as a vortex intensifies,  $2v_m/r_m$  becomes much larger than  $f$ , so that the  $f$  term in the numerator of (30) can be neglected. Then the two  $r_m$  factors in (30) cancel, yielding the approximation

$$\frac{r_m}{\ell_c} \approx \frac{2v_m}{c} = \frac{v_m}{25 \text{ m s}^{-1}}. \quad (31)$$

We conclude that, for practical purposes, the dimensionless dynamical eye radius is independent of the actual eye radius. The dimensionless dynamical eye radius depends only on  $v_m$ .

We can summarize this discussion with the following “rules of thumb.” For storms that have developed an eye but have not quite reached hurricane strength (blue curve in Fig. 9), the eye diameter is approximately two Rossby lengths and the subsidence is nearly uniform across the eye. For hurricanes that have reached an intensity of  $50 \text{ m s}^{-1}$  (boundary of Saffir-Simpson Categories 2 and 3), the eye diameter is approximately four Rossby lengths and the subsidence at the edge of the eye is 2.3 times that at the center of the eye (red curve in Fig. 9). For hurricanes that have reached an intensity of  $75 \text{ m s}^{-1}$  (Category 5), the eye diameter is approximately six Rossby lengths and the subsidence at the edge of the eye is nearly five times that at the center of the eye (green curve in Fig. 9). Thus,

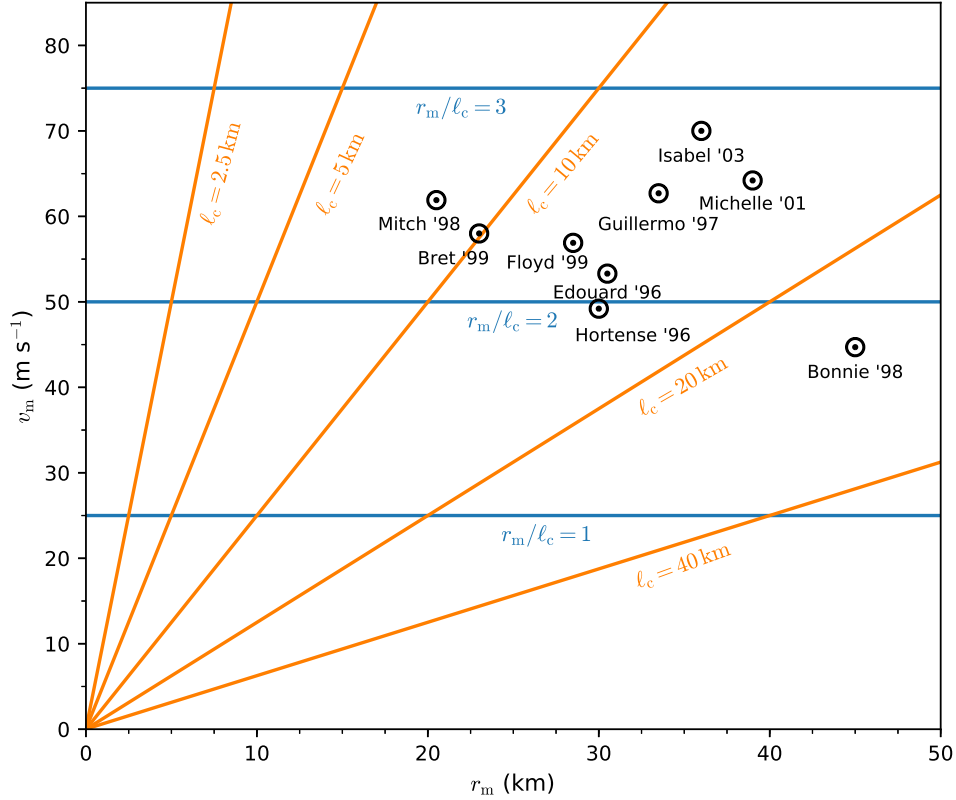


FIG. 10. The orange curves are isolines of the core Rossby length  $\ell_c$ , computed as a function of  $r_m$  and  $v_m$  from (29). The blue curves are isolines of the dimensionless dynamical eye radius  $r_m/\ell_c$ , calculated using (30). The blue curves are accurately approximated by (31). The black dots highlight examples of tropical cyclones with warm-ring thermal structures as observed by the NOAA WP-3D research aircraft.

simple balanced dynamics indicates that it is reasonable to expect that, no matter what their actual eye sizes, strong hurricanes should develop hub clouds, eye moats, and warm rings.

A survey of aircraft data taken in hurricanes with lower tropospheric warm rings reveals the nine cases indicated in Fig. 10. These hurricanes have eye diameters in the range  $38 < 2r_m < 90$  km, while their dimensionless dynamical eye diameters are generally in the range  $4 < 2r_m/\ell_c < 6$ . It should be emphasized that the simple mathematical arguments given here neglect the baroclinic effects associated with eyewall slope and consider only the vertical structure of the first internal mode. Insightful discussions of the eye subsidence and thermal structure of numerically simulated tropical cyclones can be found in Stern and Nolan (2012) and Stern and Zhang (2013).

## 5. The tropical cyclone boundary layer

We have seen in section 2 that a hollow PV tower will be produced if  $\theta$  is confined to an annular region. What dynamical process produces such a confinement? The answer appears to be that the nonlinear, frictional boundary layer dynamics of strong vortices dictate that intense boundary layer pumping, and hence large  $\theta$  in the overlying fluid, be confined to an annular region. Perhaps this is the dynamical process that Bernhard Haurwitz was seeking in the quote at the end of section 1. Although he did not discover the nonlinear dynamics discussed in this section, he did make an important contribution (Haurwitz 1935c, 1936a) to understanding the behavior of the frictional boundary layer under a specified, axisymmetric pressure field. This can be considered a classic problem in Ekman boundary layer theory, generalized in the sense that it involves highly curved flows with large Rossby numbers and with the possible formation of boundary layer shocks.<sup>9</sup> Here we simplify this problem by considering an axisym-

<sup>9</sup>For an interesting discussion of how surface friction can lead to eyewall frontogenesis, see Emanuel (1997).



metric slab boundary layer under a specified pressure field. We also consider a local, steady state model that is an approximation of the original model. The local model neglects the local time derivative terms, the horizontal diffusion terms, the vertical advection terms, and the radial advection of radial velocity; it also makes selective use of the gradient wind approximation.

Both models consider axisymmetric, boundary layer motions of an incompressible fluid on an  $f$ -plane. The frictional boundary layer is assumed to have constant density  $\rho$  and constant depth  $h$ , with radial and azimuthal velocities  $u(r, t)$  and  $v(r, t)$  that are independent of height between the top of a thin surface layer and height  $h$ , and with vertical velocity  $w(r, t)$  at height  $h$ . In the overlying layer, the radial velocity is assumed to be negligible and the azimuthal velocity  $v_{\text{gr}}(r, t)$  is assumed to be in gradient balance and to be a specified function of radius and time. The boundary layer flow is driven by the same radial pressure gradient force that occurs in the overlying fluid. The governing system of differential equations for the boundary layer variables  $u(r, t)$ ,  $v(r, t)$ , and  $w(r, t)$  then takes the form

$$\frac{\partial u}{\partial t} + u \frac{\partial u}{\partial r} - \frac{w}{h}(1-\alpha)u - \left(f + \frac{v}{r}\right)v + \frac{1}{\rho} \frac{\partial p}{\partial r} = -\frac{c_d U}{h} u + K \frac{\partial}{\partial r} \left( \frac{\partial(ru)}{r \partial r} \right), \quad (32)$$

$$\frac{\partial v}{\partial t} + u \frac{\partial v}{\partial r} - \frac{w}{h}(1-\alpha)(v - v_{\text{gr}}) + \left(f + \frac{v}{r}\right)u = -\frac{c_d U}{h} v + K \frac{\partial}{\partial r} \left( \frac{\partial(rv)}{r \partial r} \right), \quad (33)$$

$$w = -h \frac{\partial(ru)}{r \partial r} \quad \text{and} \quad \alpha = \begin{cases} 1 & \text{if } w \geq 0 \\ 0 & \text{if } w < 0, \end{cases} \quad (34)$$

where  $f$  is the constant Coriolis parameter,  $K$  the constant horizontal diffusivity, and  $U = k(u^2 + v^2)^{1/2}$  the surface wind speed, with  $k$  chosen to be 0.78. The boundary layer velocity field is driven by the specified pressure field  $p(r, t)$  in (32). However, it is more convenient to specify this forcing in terms of the associated gradient wind field  $v_{\text{gr}}(r, t)$ , which is related to  $p(r, t)$  via the gradient wind formula

$$\left(f + \frac{v_{\text{gr}}}{r}\right)v_{\text{gr}} = \frac{1}{\rho} \frac{\partial p}{\partial r}. \quad (35)$$

In the absence of the horizontal diffusion terms, the slab boundary layer equations constitute a hyperbolic system that can be written in characteristic form (Slocum et al. 2014). A knowledge of the characteristic form is useful in understanding the formation of shocks. Before presenting numerical solutions of the system (32)–(34), we present a local model which proves to give accurate results at all radii except near the radius of shock formation.

The local, steady state approximation is derived by first neglecting the  $(\partial/\partial t)$ -terms, the horizontal diffusion terms, and the  $w$ -terms in (32) and (33). The resulting equations can then be written in the form<sup>10</sup>

$$\begin{aligned} u \frac{\partial u}{\partial r} - (f + \zeta)v + \frac{c_d U}{h} u &= -\frac{\partial}{\partial r} \left( \frac{p}{\rho} + \frac{1}{2} v^2 \right), \\ (f + \zeta)u + \frac{c_d U}{h} v &= 0, \end{aligned} \quad (36)$$

where the boundary layer relative vorticity is defined by  $\zeta = \partial(rv)/r \partial r$ . Next, approximate  $f + \zeta$  by  $f + \zeta_{\text{gr}}$ , and approximate  $(p/\rho) + \frac{1}{2} v^2$  by  $(p/\rho) + \frac{1}{2} v_{\text{gr}}^2$ , thereby obtaining

$$\begin{aligned} u \frac{\partial u}{\partial r} - (f + \zeta_{\text{gr}})v + \frac{c_d U}{h} u &= -(f + \zeta_{\text{gr}})v_{\text{gr}}, \\ (f + \zeta_{\text{gr}})u + \frac{c_d U}{h} v &= 0, \end{aligned} \quad (37)$$

where the relative vorticity of the gradient wind is defined by  $\zeta_{\text{gr}} = \partial(rv_{\text{gr}})/r \partial r$ , and where we have made use of (35). The final step in the derivation of the local model is to neglect the  $u(\partial u/\partial r)$  term in the top line of (37). This removes the nonlocal nature of (37) and results in the local model equations

$$\begin{aligned} -(f + \zeta_{\text{gr}})v + \left( \frac{k c_d (u^2 + v^2)^{1/2}}{h} \right) u &= -(f + \zeta_{\text{gr}})v_{\text{gr}}, \\ (f + \zeta_{\text{gr}})u + \left( \frac{k c_d (u^2 + v^2)^{1/2}}{h} \right) v &= 0. \end{aligned} \quad (38)$$

<sup>10</sup>Interesting discussions of steady state models similar to (36) are given by Smith and Vogl (2008) and Kepert (2010a,b).

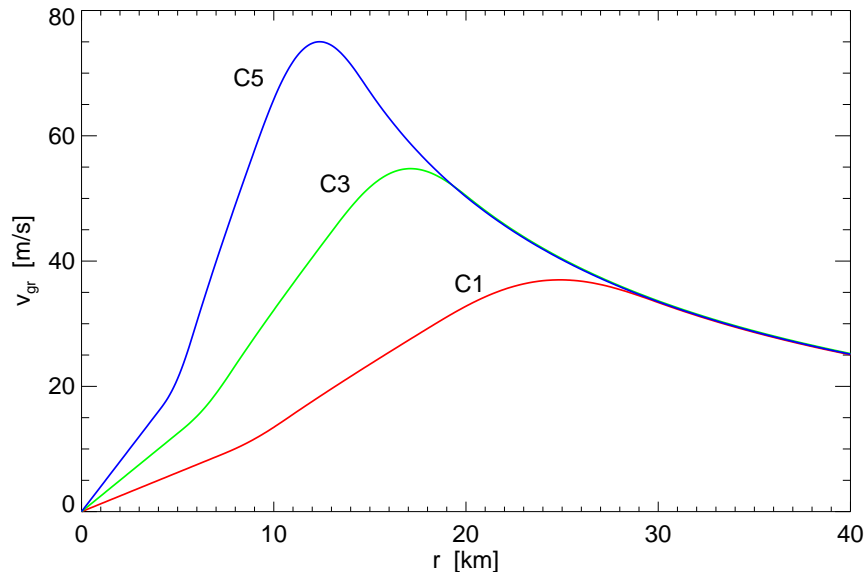


FIG. 11. Radial profiles of  $v_{\text{gr}}$  for the category 1, 3, and 5 cases. From Williams et al. (2013).

Given a radial profile  $v_{\text{gr}}(r)$  and its associated vorticity  $\zeta_{\text{gr}}(r)$ , we can solve the nonlinear equations (38) for  $u$  and  $v$  at each radial point.

Figure 11 shows  $v_{\text{gr}}(r)$  profiles for the three vortices studied by Williams et al. (2013). The maximum values of the gradient wind  $v_{\text{gr}}(r)$  for the Category 1, 3, and 5 cases are 37.5, 55, and 75  $\text{m s}^{-1}$ , respectively. Numerical integration<sup>11</sup> of (32)–(34) shows that in all three cases, the vortices quickly evolve into a nearly steady state, with small changes after 2 or 3 hours. Figure 12 shows  $u$ ,  $v$ ,  $w$ , and  $\zeta$  for  $t = 0$  and  $t = 3$  hours for each category vortex. An interesting feature of the radial profiles of  $w(r, t)$  is the very sharp gradient on the inner side and the relatively slower decrease on the outer side of the maximum. Through the mass continuity equation (34), this behaviour of  $w(r, t)$  is related to the shock-like structure<sup>12</sup> of  $u(r, t)$ . To a certain extent, the radial structure of  $w(r, t)$  in the slab model agrees with the observed radial structure in the famous Hurricane Hugo case, which is shown in Fig. 13. Another interesting feature of the Category 3 and 5 cases is the rather large boundary layer pumping that the slab model produces, when compared with the observations of Fig. 13. Some of this discrepancy is probably due to the simplicity of the slab model and the chosen value of  $K$ , but some may be explained by the low elevation of the flight level for the red curve in the lower panel of Fig. 13, i.e., there may have been radially convergent flow above flight level so that a larger  $w$  might have been measured if the aircraft had flown several hundred meters higher. In actual hurricanes, this shock effect makes the inner core boundary layer a dangerous place for research aircraft. The location of shock formation also plays a crucial role in determining the eyewall radius, and hence where the diabatic heating will occur relative to the region of high inertial stability.

Although not shown here, the solutions of the local model (38) are close to the solutions of the non-local model (32)–(34), except near the region of the shock. In this region, the local model is inaccurate, primarily because of the neglect of the  $u(\partial u/\partial r)$  term. Thus, it is the nonlinear dynamics of the boundary layer that determines the location of the eyewall and hence the diameter of the eye.

## 6. The formation of PV anomalies in the ITCZ

In this section, we discuss the strong analogy between the PV dynamics of the ITCZ and the PV dynamics of a tropical cyclone. As in a tropical cyclone, there are transient inertia-gravity waves in the ITCZ, but a useful idealization is that the ITCZ is essentially a balanced, PV phenomenon, with the balanced wind and mass fields invertible from the PV field. Again, with frictional effects confined primarily to a shallow boundary layer, the evolution of PV above the boundary layer is determined by advection and diabatic effects. Considering zonally symmetric, inviscid flow on the

<sup>11</sup>The formula used to describe the dependence of  $c_{\text{D}}$  on  $U$  is given in Williams et al. (2013).

<sup>12</sup>Here we are using the term “shock” rather than the term “front”, because the near discontinuity in  $u$  arises from  $u(\partial u/\partial r)$ , i.e., the advection of the divergent wind component by the divergent wind component. This term is neglected in the accepted semi-geostrophic theory of line-symmetric atmospheric fronts.

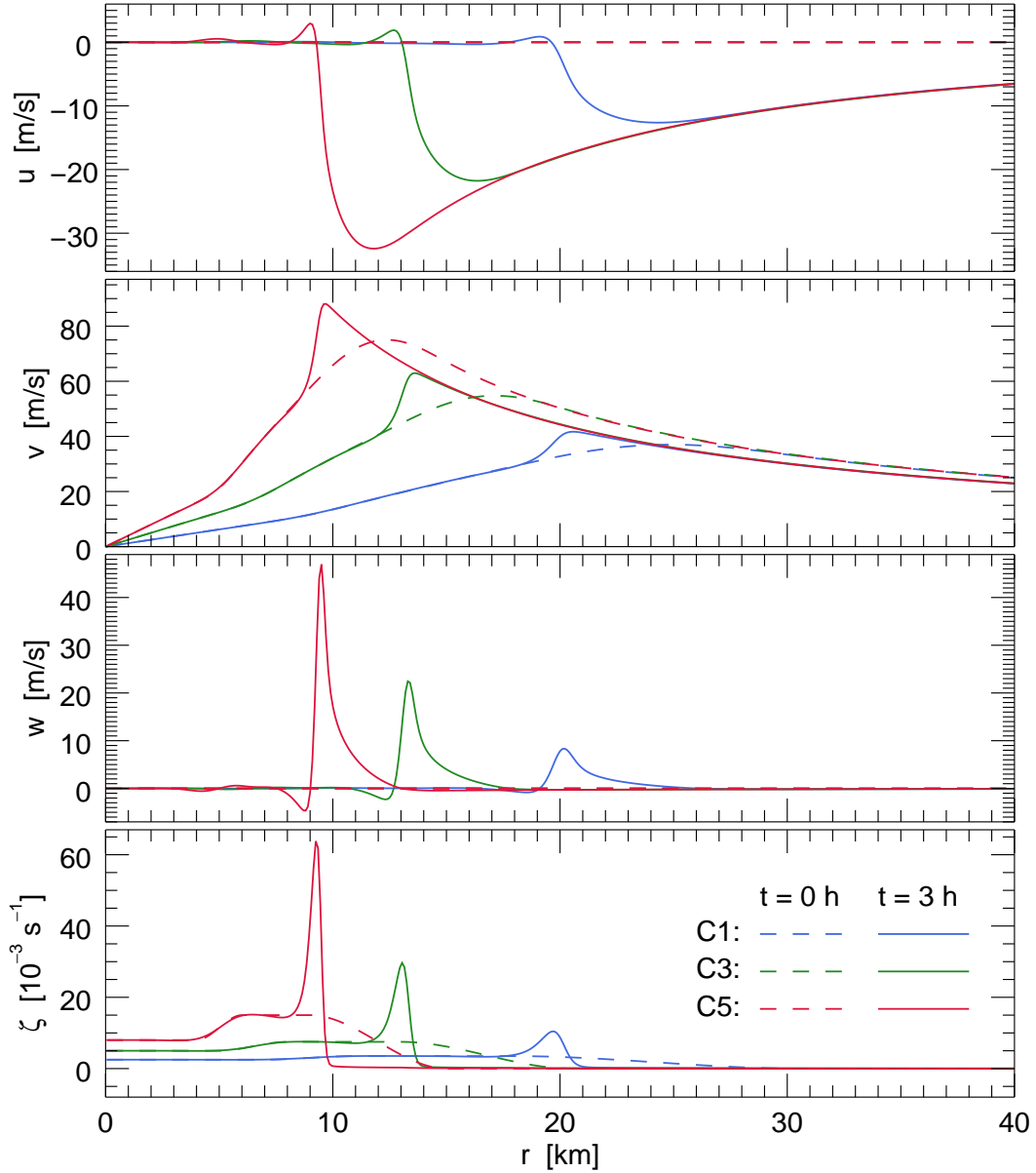


FIG. 12. Steady-state (i.e.,  $t = 3$  hours) slab boundary layer results for the C1, C3, and C5 forcing cases. From Williams et al. (2013).

sphere, and using latitude  $\phi$ , height  $z$ , and time  $t$  as the independent variables, the PV equation takes the form

$$\frac{\partial P}{\partial t} + v \frac{\partial P}{a \partial \phi} + w \frac{\partial P}{\partial z} = \frac{1}{\rho} \left[ \frac{\partial u}{\partial z} \frac{\partial \dot{\theta}}{a \partial \phi} + \left( 2\Omega \sin \phi - \frac{\partial(u \cos \phi)}{a \cos \phi \partial \phi} \right) \frac{\partial \dot{\theta}}{\partial z} \right], \quad (39)$$

where  $u$  is the zonal velocity,  $v$  the meridional velocity,  $w$  the vertical velocity,  $\rho$  the density,  $\dot{\theta}$  the diabatic heating, and where the potential vorticity is given by

$$P = \frac{1}{\rho} \left[ \frac{\partial u}{\partial z} \frac{\partial \theta}{a \partial \phi} + \left( 2\Omega \sin \phi - \frac{\partial(u \cos \phi)}{a \cos \phi \partial \phi} \right) \frac{\partial \theta}{\partial z} \right] = \frac{2\Omega \sin \Phi}{\rho} \frac{\partial(\sin \Phi, \theta)}{\partial(\sin \phi, z)}, \quad (40)$$

with the potential latitude  $\Phi$  defined in terms of the absolute angular momentum by  $\Omega a \cos^2 \Phi = u \cos \phi + \Omega a \cos^2 \phi$ . We will now collapse the partial differential equation (39) into two simple ordinary differential equations, which can

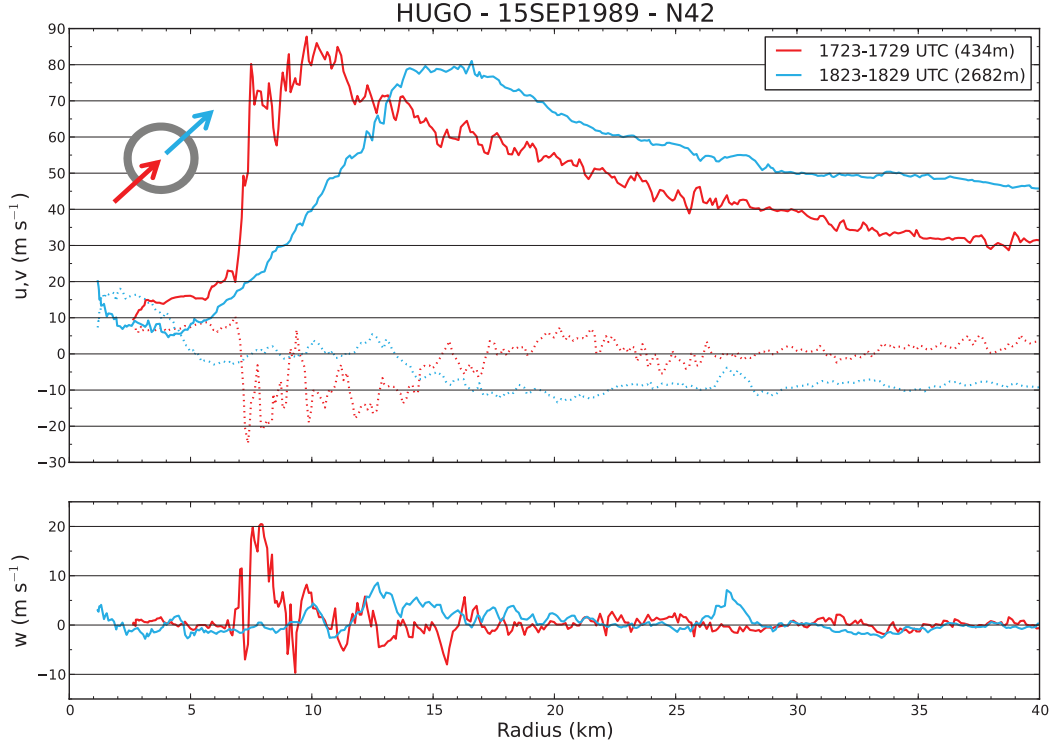


FIG. 13. The top panel shows NOAA WP-3D aircraft data from an inbound leg in the southwest quadrant (red, 434 m average height) and an outbound leg in the northeast quadrant (blue, 2682 m average height) for Hurricane Hugo on 15 September 1989. The solid curves show the tangential wind component, while the dotted curves show the radial wind component. The bottom panel shows the vertical velocity. The shock-like feature in the boundary layer (434 m height) occurs at a radius of 7–8 km. From Williams et al. (2013).

be solved analytically. To accomplish this simplification, first transform from the original independent variables  $(\phi, z, t)$  to the new independent variables  $(\Phi, \theta, \tau)$ , where  $\tau = t$ , but  $\partial/\partial\tau$  means that  $\Phi$  and  $\theta$  are fixed, while  $\partial/\partial t$  means that  $\phi$  and  $z$  are fixed. Then, the  $(\phi, z, t)$ -form of the material derivative is related the  $(\Phi, \theta, \tau)$ -form by

$$\frac{\partial}{\partial t} + v \frac{\partial}{a \partial \phi} + w \frac{\partial}{\partial z} = \frac{\partial}{\partial \tau} + \dot{\Phi} \frac{\partial}{\partial \Phi} + \dot{\theta} \frac{\partial}{\partial \theta}, \quad (41)$$

where  $\dot{\Phi}$  is the rate that fluid particles are crossing  $\Phi$ -surfaces. For inviscid zonally symmetric flow, the absolute angular momentum is materially conserved, so that  $\dot{\Phi} = 0$ , which simplifies the right-hand side of (41) and hence the left-hand side of (39). The right-hand side of (39) can also be simplified by writing it as

$$\begin{aligned} & \frac{1}{\rho} \left[ \frac{\partial u}{\partial z} \frac{\partial \dot{\theta}}{a \partial \phi} + \left( 2\Omega \sin \phi - \frac{\partial(u \cos \phi)}{a \cos \phi \partial \phi} \right) \frac{\partial \dot{\theta}}{\partial z} \right] \\ &= \frac{2\Omega \sin \Phi}{\rho} \frac{\partial(\sin \Phi, \dot{\theta})}{\partial(\sin \phi, z)} = \frac{2\Omega \sin \Phi}{\rho} \frac{\partial(\sin \Phi, \theta)}{\partial(\sin \phi, z)} \frac{\partial(\sin \Phi, \dot{\theta})}{\partial(\sin \Phi, \theta)} = P \frac{\partial \dot{\theta}}{\partial \theta}, \end{aligned} \quad (42)$$

where the second equality makes use of the Jacobian chain rule and the third equality makes use of (40). Then, using (41) and (42) in (39), the PV equation becomes

$$\frac{\partial P}{\partial \tau} + \dot{\theta} \frac{\partial P}{\partial \theta} = P \frac{\partial \dot{\theta}}{\partial \theta}. \quad (43)$$

The PV dynamics (43), which is equivalent to (39), can now be written in the characteristic form

$$\frac{d \ln P}{d \tau} = \frac{\partial \dot{\theta}}{\partial \theta} \quad \text{on} \quad \frac{d \theta}{d \tau} = \dot{\theta}, \quad (44)$$

where  $(d/d\tau) = (\partial/\partial\tau) + \dot{\theta}(\partial/\partial\theta)$  is the derivative along the characteristic. As in the tropical cyclone case (section 2) the pair of ordinary differential equations in (37) can be solved sequentially, i.e., the second can be solved for the shapes of the characteristics and then the first can be solved for the variation of PV along the characteristics. Since (43) is identical to (5), and since (44) is identical to (6), the PV dynamics along a potential radius surface in a tropical cyclone is identical to the PV dynamics along a potential latitude surface in the ITCZ. However, two important differences are the inclusion of variable Coriolis parameter in the ITCZ case and the rates at which the PV evolves. Since the values of  $\dot{\theta}$  in a tropical cyclone eyewall are so much larger than in the ITCZ, the  $\tau_c$ -clock for an  $R$ -surface in a tropical cyclone eyewall generally runs much faster than the  $\tau_c$ -clock for a  $\Phi$ -surface in the ITCZ.

For the example considered here, we assume that  $\dot{\theta}$  is independent of  $\tau$  and has the separable form

$$\dot{\theta}(\Phi, \theta) = \dot{\Theta}(\Phi) \sin^2 \left( \frac{\pi(\theta - \theta_B)}{\theta_T - \theta_B} \right), \quad (45)$$

where  $\dot{\Theta}(\Phi)$  is a specified function, and where the bottom and top isentropes are again chosen as  $\theta_B = 300$  K and  $\theta_T = 360$  K. This  $\sin^2$  profile produces PV anomalies that are entirely internal since  $\partial\dot{\theta}/\partial\theta$  vanishes at  $\theta = \theta_B, \theta_T$ . This is probably more appropriate when there is a significant fraction of stratiform precipitation that produces evaporative cooling near the surface.

Using (45) in the second equation of (44), we obtain

$$\frac{\left(\frac{\pi}{\theta_T - \theta_B}\right) d\theta}{\sin^2 \left( \frac{\pi(\theta - \theta_B)}{\theta_T - \theta_B} \right)} = d\tau_c, \quad \text{where} \quad \tau_c = \frac{\pi\dot{\Theta}(\Phi)\tau}{\theta_T - \theta_B}. \quad (46)$$

As in the hurricane case, this dimensionless convective clock runs at different rates on different  $\Phi$ -surfaces. In the center of the ITCZ, where  $\dot{\Theta}(\Phi)$  is large, the  $\tau_c$ -clock advances quickly, while near the edge of the ITCZ, the  $\tau_c$ -clock advances slowly, or not at all. Integration of (46) yields the characteristic equation

$$\theta(\vartheta, \tau_c) = \theta_B + \frac{(\theta_T - \theta_B)}{\pi} \cot^{-1} \left[ \cot \left( \frac{\pi(\vartheta - \theta_B)}{\theta_T - \theta_B} \right) - \pi\tau_c \right], \quad (47)$$

where  $\vartheta$  is the label of the characteristic, i.e., the initial potential temperature of the characteristic. To confirm that (47) satisfies the initial condition, note that the  $\pi\tau_c$  factor becomes zero when  $\tau_c = 0$  and that the inverse cotangent and cotangent operations then cancel, so that (47) reduces to  $\theta = \vartheta$  when  $\tau_c = 0$ . The red curves in Fig. 14 are the characteristics  $\theta(\vartheta, \tau_c)$  given by (47). These characteristics bend upward most rapidly at  $\theta = 330$  K, where the value of  $\dot{\theta}$  is largest. As in section 2, it is useful to rearrange (47) into the form

$$\vartheta(\theta, \tau_c) = \theta_B + \frac{\theta_T - \theta_B}{\pi} \cot^{-1} \left[ \cot \left( \frac{\pi(\theta - \theta_B)}{\theta_T - \theta_B} \right) + \pi\tau_c \right], \quad (48)$$

which can be regarded as giving the initial potential temperature of the characteristic that goes through the point  $(\theta, \tau_c)$ .

We now turn our attention to the solution of the first ordinary differential equation in (44). With the previous assumption (45) that  $\dot{\theta}$  depends only on  $(\Phi, \theta)$ , and now assuming that the initial potential vorticity is  $P_0 \sin \Phi$ , where  $P_0$  is a constant, the solution of the first equation in (44) is

$$P(\Phi, \theta, \tau_c) = P_0 \sin \Phi \left( \frac{\dot{\theta}(\Phi, \theta)}{\dot{\theta}(\Phi, \vartheta(\theta, \tau_c))} \right). \quad (49)$$

Using (45) and (48) in (49), we obtain the final solution

$$\frac{P(\Phi, \theta, \tau_c)}{P_0} = \sin \Phi \left( \frac{\sin^2 \left( \frac{\pi(\theta - \theta_B)}{\theta_T - \theta_B} \right)}{\sin^2 \left\{ \cot^{-1} \left[ \cot \left( \frac{\pi(\theta - \theta_B)}{\theta_T - \theta_B} \right) + \pi\tau_c(\Phi) \right] \right\}} \right). \quad (50)$$

Although the right-hand side of (50) is indeterminate at the boundaries, use of L'Hospital's rule yields  $P(\theta, \Phi, \tau_c) = P_0 \sin \Phi$  at  $\theta = \theta_B, \theta_T$ .

Isolines of the dimensionless potential vorticity  $P(\theta, \Phi, \tau_c)/P_0 \sin \Phi$  are shown by the blue curves in Fig. 14. The largest values of PV occur at  $\tau_c = 2.5$  on midtropospheric isentropes. In the region  $300 \leq \theta \leq 330$  K, both the

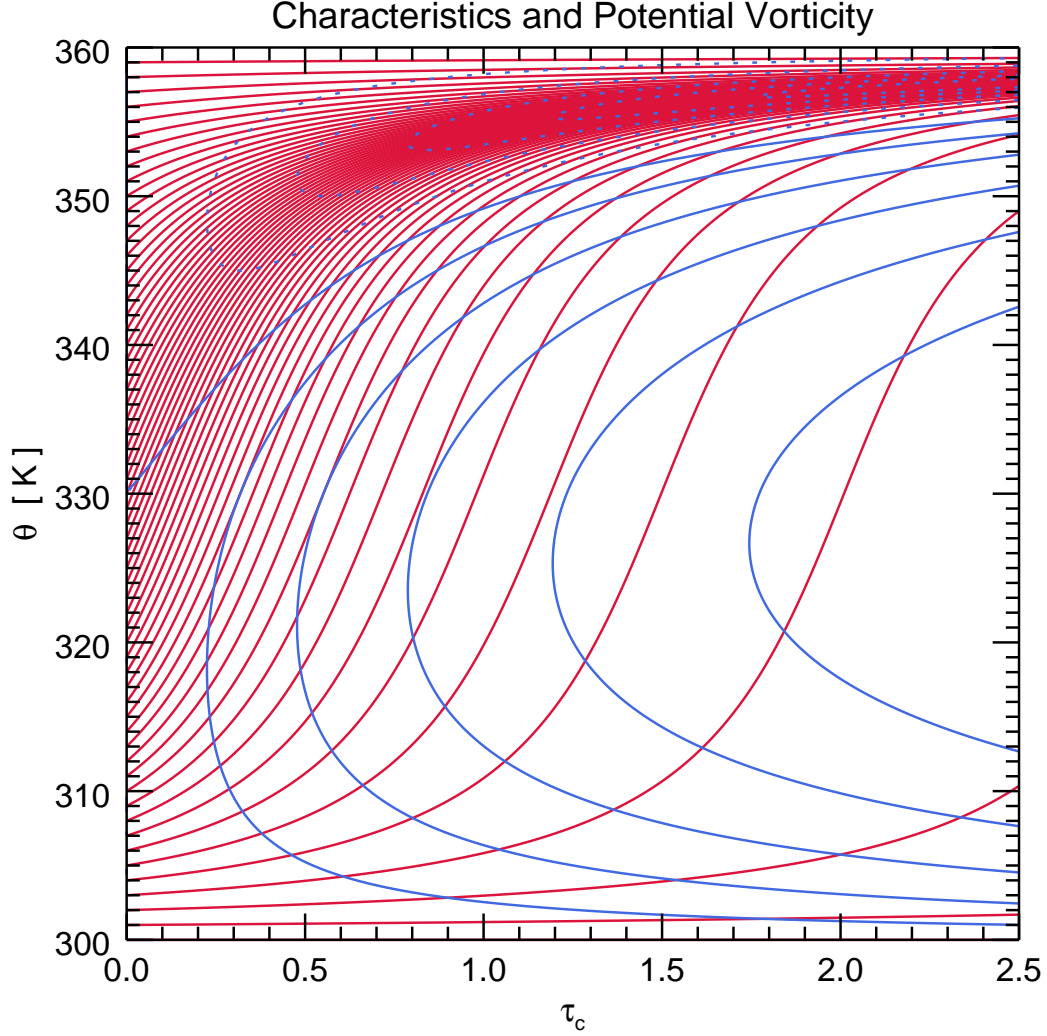


FIG. 14. The red curves are the characteristics  $\theta(\vartheta, \tau_c)$  determined from (47), with  $\vartheta$  denoting the characteristic label (i.e., the initial value of the potential temperature) and  $\tau_c$  denoting the dimensionless convective clock defined in the second entry of (46). The blue curves are isolines of  $P(\theta, \tau_c)/P_0 \sin \Phi$ , as determined from (50). The blue isoline starting at 330 K corresponds to  $P(\theta, \tau_c)/P_0 \sin \Phi = 1$ , with the other solid isolines corresponding to  $P(\theta, \tau_c)/P_0 \sin \Phi = 2, 4, 8, 16, 32$  and the dashed lines corresponding to  $P(\theta, \tau_c)/P_0 \sin \Phi = 1/2, 1/4, 1/8, 1/16$ .

$\dot{\theta}(\partial P/\partial \theta)$  and the  $P(\partial \dot{\theta}/\partial \theta)$  terms in (43) contribute to positive  $(\partial P/\partial \tau)$ . In the region  $330 \leq \theta \leq 360$  K, the  $P(\partial \dot{\theta}/\partial \theta)$ -term makes a negative contribution to  $(\partial P/\partial \tau)$ , but  $(\partial P/\partial \tau)$  remains positive because of the  $\dot{\theta}(\partial P/\partial \theta)$ -term. The net effect is that a tower of high PV grows into the upper troposphere.

To get a better appreciation of the formation of a PV anomaly in the ITCZ, consider the example  $\dot{\Theta}(\Phi) = \dot{\Theta}_m \exp[-(\Phi - \Phi_m)^2/\Phi_w^2]$ , where  $\Phi_m$  is the potential latitude of the maximum diabatic heating (center of the ITCZ),  $\Phi_w$  is the width of the diabatic heating, and  $\dot{\Theta}_m$  is the maximum value of  $\dot{\Theta}(\Phi)$ . Using this  $\dot{\Theta}(\Phi)$  in the second entry of (46), we obtain

$$\tau_c(\Phi) = \tau_c(\Phi_m) \exp\left(-\frac{(\Phi - \Phi_m)^2}{\Phi_w^2}\right), \quad \text{where} \quad \tau_c(\Phi_m) = \frac{\pi \dot{\Theta}_m \tau}{\theta_T - \theta_B}. \quad (51)$$

Using (51) in (50), we can now produce  $(\Phi, \theta)$ -cross-sections of PV at different times. Figure 15 shows isolines of PV in  $(\Phi, \theta)$ -space for the choice  $\Phi_m = 10^\circ$ ,  $\Phi_w = 2^\circ$  and for the three times  $\tau_c(\Phi_m) = \pi/16, 3\pi/32, \pi/8$ . Note that a mini-tower of PV is produced.<sup>13</sup>

<sup>13</sup>For additional discussion, see Schubert et al. (1991).

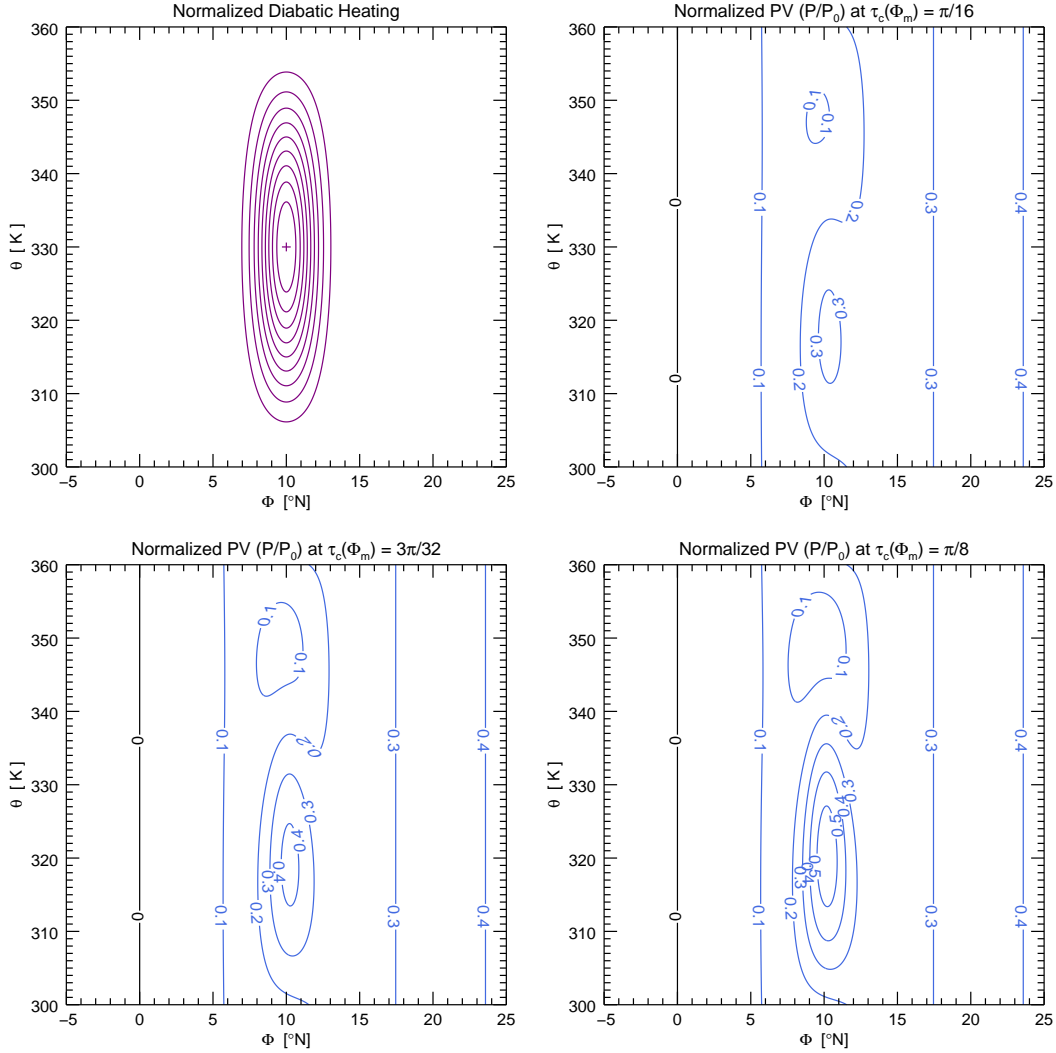


FIG. 15. The upper left panel shows isolines of  $\hat{\theta}(\Phi, \theta)/\hat{\Theta}_m$ . The remaining three panels show isolines of  $P(\Phi, \theta, \tau_c)/P_0$ , as determined from (50) and (51), for  $\Phi_m = 10^\circ$ ,  $\Phi_w = 2^\circ$ , and for the three times corresponding to  $\tau_c(\Phi_m) = \pi/16, 3\pi/32, \pi/8$ .

Since zonally symmetric PV anomalies develop within a background state that has potential vorticity increasing to the north, reversed poleward gradients of potential vorticity are produced. For typical diabatic heating rates, significant PV gradient reversals can occur within a couple of days. This sets the stage for combined barotropic-baroclinic instability and the growth of easterly waves. The barotropic aspects of this instability process are discussed by Nieto Ferreira and Schubert (1997), who used a global shallow water model. More detailed simulations have been made by Magnusdottir and Wang (2008) and Wang and Magnusdottir (2005, 2006), using a multi-level global spectral model. In a companion observational study Bain et al. (2011) have developed objective methods for detecting the ITCZ using instantaneous satellite data and have produced an ITCZ climatology for the east Pacific.

It should be noted that this PV interpretation of the ITCZ and Hadley circulation is quite different than the interpretations of Schneider and Lindzen (1977), Schneider (1977), Held and Hou (1980), and Lindzen and Hou (1988), all of whom seek steady state solutions for the forced, zonally symmetric flow. In the present analysis, the diabatic heating  $\hat{\theta}$  results in a continuously evolving PV field, so a steady state is never reached. However, the evolving flow field does become unstable to combined barotropic-baroclinic instability.

## 7. Concluding remarks

The concepts presented here, involving the formation of PV towers in both tropical cyclones and the ITCZ, are quite different from those presented a half century ago by Charney and Eliassen (1964) and Charney (1971). The older view was that the basic dynamics of both tropical cyclones and the ITCZ could be understood through linear stability analyses involving balanced models with parameterized convection. For unstable disturbances, the primary circulation, the secondary circulation, and the diabatic heating all increase exponentially with time. The modern view is that a better understanding is obtained through analysis of the nonlinear aspects of the PV evolution. In this view the primary circulation can increase exponentially in time while the diabatic heating is fixed. The modern view also recognizes that the nonlinear dynamics of the boundary layer produces the sharp, intense boundary layer pumping that dictates the position of the eyewall and the size of the eye. A major challenge for future research is to improve intensity forecasting by improving numerical simulation of the tropical cyclone's mesoscale power plant. Just how much improvement is possible remains unknown, since there are no doubt some basic limitations to the predictability of tropical cyclone intensity.

For those interested in further information about the life of Bernhard Haurwitz, there are several excellent sources. The first is his own series of four short articles entitled "Meteorology in the 20th Century—A Participant's View," published in the *Bulletin of the American Meteorological Society* (1985). The second is the National Academy of Sciences Biographical Memoir written by his longtime colleague Julius London (1996). The third is an extensive transcribed interview entitled "Conversations with Bernhard Haurwitz," conducted by master interviewer George Platzman (1985). Finally, there is an excellent historical article, also by Platzman (1996), on the diurnal tide in surface pressure, entitled "The S-1 Chronicle: A Tribute to Bernhard Haurwitz."

## Acknowledgements

I would like to thank Rick Taft and Chris Slocum for their help in preparing this Bernhard Haurwitz Memorial Lecture. I would also like to thank the AMS for their continuing support of this lecture series since its inception in 1989. The author's research is supported by the National Science Foundation under Grants AGS-1546610 and AGS-1601623.

## References

- Aberson, S. D., M. T. Montgomery, M. M. Bell, and M. Black, 2006: Hurricane Isabel (2003): New insights into the physics of intense storms. Part II: Extreme localized wind. *Bull. Amer. Meteor. Soc.*, **87**, 1349–1354.
- Bain, C. L., J. De Paz, J. Kramer, G. Magnusdottir, P. Smyth, H. Stern, and C.-C. Wang, 2011: Detecting the ITCZ in instantaneous satellite data using spatiotemporal statistical modeling: ITCZ climatology in the east Pacific. *J. Climate*, **24**, 216–230.
- Bell, M. M., J. Martinez, J. Doyle, and R. Rogers, 2017: Inner core structure of Hurricane Patricia observed during TCI-2015, Presented at JpGU–AGU Joint Meeting, Chiba, Japan, May 20–25, 2017.
- Bell, M. M., and M. T. Montgomery, 2008: Observed structure, evolution, and potential intensity of category 5 Hurricane Isabel (2003) from 12 to 14 September. *Mon. Wea. Rev.*, **136**, 2023–2046.
- Bjerknes, J., 1937: Theorie der aussertropischen Zyklonenbildung. *Meteor. Z.*, **54**, 462–466.
- Blandford, R. R., 1966: Mixed gravity-Rossby waves in the ocean. *Deep-Sea Res.*, **13**, 941–961.
- Charney, J. G., 1971: Tropical cyclogenesis and the formation of the Intertropical Convergence Zone. *Mathematical Problems in the Geophysical Sciences: I. Geophysical Fluid Dynamics*, Lectures in Applied Mathematics, Volume 13, American Mathematical Society, 355–368.
- Charney, J. G., and A. Eliassen, 1964: On the growth of the hurricane depression. *J. Atmos. Sci.*, **21**, 68–75.
- Ehrmann, W., and M. Wendisch (Eds.), 2013: *Geophysics and Meteorology at the University of Leipzig*. Leipziger Universitätsverlag GmbH, 111 pp.
- Ekman, V. W., 1923: Über horizontalzirkulation bei winderzeugten meeresströmungen. *Arkiv för Mat. Astron. och Fysik*, **17**, 74.



- Ekman, V. W., 1932: Studien zur dynamik der meeresströmungen. *Gerlands Beitr. Geophys.*, **36**, 385–438.
- Emanuel, K. A., 1997: Some aspects of hurricane inner-core dynamics and energetics. *J. Atmos. Sci.*, **54**, 1014–1026.
- Emanuel, K. A., 2005: *Divine Wind: The History and Science of Hurricanes*. Oxford University Press, 296 pp.
- Fine, K. S., A. C. Cass, W. G. Flynn, and C. F. Driscoll, 1995: Relaxation of 2D turbulence to vortex crystals. *Phys. Rev. Lett.*, **75**, 3277–3280.
- Guinn, T. A., 1992: A Dynamical Theory for Hurricane Spiral Bands. Ph.D. thesis, Dept. of Atmos. Sci., Colorado State University, 178 pp.
- Haltiner, G. J., and F. L. Martin, 1957: *Dynamical and Physical Meteorology*. McGraw-Hill Book Company, 470 pp.
- Haurwitz, B., 1935a: A theoretical study of wind-velocity and wind-direction in curved air-currents. *Trans. Amer. Geophys. Union*, **16**, 124–126.
- Haurwitz, B., 1935b: The height of tropical cyclones and of the “eye” of the storm. *Mon. Wea. Rev.*, **63**, 45–49.
- Haurwitz, B., 1935c: On the change of the wind with elevation under the influence of viscosity in curved air currents. *Gerlands Beitr. Geophys.*, **45**, 243–267.
- Haurwitz, B., 1936a: Supplementary to: On the change of the wind with elevation under the influence of viscosity in curved air currents. *Gerlands Beitr. Geophys.*, **47**, 203–205.
- Haurwitz, B., 1936b: On the vertical wind distribution in anticyclones, extratropical and tropical cyclones under the influence of eddy viscosity. *Gerlands Beitr. Geophys.*, **47**, 206–214.
- Haurwitz, B., 1936c: On the structure of tropical cyclones. *Quart. J. Roy. Meteor. Soc.*, **62**, 145–146.
- Haurwitz, B., 1937: The oscillations of the atmosphere. *Gerlands Beitr. Geophys.*, **51**, 195–233.
- Haurwitz, B., 1940a: The motion of atmospheric disturbances. *J. Mar. Res.*, **3**, 35–50.
- Haurwitz, B., 1940b: The motion of atmospheric disturbances on the spherical earth. *J. Mar. Res.*, **3**, 254–267.
- Haurwitz, B., 1951: The motion of binary tropical cyclones. *Arch. Meteorol. Geophys. Bioklim.*, **A4**, 73–86.
- Haurwitz, B., 1985: Meteorology in the 20th Century—A Participant's View. *Bull. Amer. Meteor. Soc.*, **66**, 281–291, 424–431, 498–504, 628–633.
- Held, I. M., and A.-Y. Hou, 1980: Nonlinear axially symmetric circulations in a nearly inviscid atmosphere. *J. Atmos. Sci.*, **37**, 515–533.
- Hendricks, E. A., B. D. McNoldy, and W. H. Schubert, 2012: Observed inner-core structural variability in Hurricane Dolly (2008). *Mon. Wea. Rev.*, **140**, 4066–4077.
- Hendricks, E. A., and W. H. Schubert, 2010: Adiabatic rearrangement of hollow PV towers. *J. Adv. Model. Earth Syst.*, **2**, Article 8.
- Hendricks, E. A., W. H. Schubert, Y.-H. Chen, H.-C. Kuo, and M. S. Peng, 2014: Hurricane eyewall evolution in a forced shallow-water model. *J. Atmos. Sci.*, **71**, 1623–1643.
- Hendricks, E. A., W. H. Schubert, R. K. Taft, H. Wang, and J. P. Kossin, 2009: Life cycles of hurricane-like vorticity rings. *J. Atmos. Sci.*, **66**, 705–722.
- Hough, S. S., 1897: On the application of harmonic analysis to the dynamical theory of the tides. Part I: On Laplace's “oscillations of the first species” and the dynamics of ocean currents. *Philos. Trans. Roy. Soc. London A*, **189**, 201–257.
- Hough, S. S., 1898: On the application of harmonic analysis to the dynamical theory of the tides. Part II: On the general integration of Laplace's dynamical equations. *Philos. Trans. Roy. Soc. London A*, **191**, 139–185.

- Judt, E., and S. S. Chen, 2010: Convectively generated potential vorticity in rainbands and formation of the secondary eyewall in Hurricane Rita of 2005. *J. Atmos. Sci.*, **67**, 3581–3599.
- Kepert, J. D., 2010a: Comparing slab and height-resolving models of the tropical cyclone boundary layer. Part I: Comparing the simulations. *Quart. J. Roy. Meteor. Soc.*, **136**, 1689–1699.
- Kepert, J. D., 2010b: Comparing slab and height-resolving models of the tropical cyclone boundary layer. Part II: Why the simulations differ. *Quart. J. Roy. Meteor. Soc.*, **136**, 1700–1711.
- Kossin, J. P., and M. D. Eastin, 2001: Two distinct regimes in the kinematic and thermodynamic structure of the hurricane eye and eyewall. *J. Atmos. Sci.*, **58**, 1079–1090.
- Kossin, J. P., and W. H. Schubert, 2001: Mesovortices, polygonal flow patterns, and rapid pressure falls in hurricane-like vortices. *J. Atmos. Sci.*, **58**, 2196–2209.
- Kossin, J. P., and W. H. Schubert, 2004: Mesovortices in Hurricane Isabel. *Bull. Amer. Meteor. Soc.*, **85**, 151–153.
- Kwon, Y., and W. M. Frank, 2005: Dynamic instabilities of simulated hurricane-like vortices and their impacts on the core structure of hurricanes. Part I: Dry dynamics. *J. Atmos. Sci.*, **62**, 3955–3973.
- Lahaye, N., and V. Zeitlin, 2016: Understanding instabilities of tropical cyclones and their evolution with a moist convective rotating shallow-water model. *J. Atmos. Sci.*, **73**, 505–523.
- Laplace, P. S., 1799–1827: *Traité de mécanique céleste, Volumes I–V*. First four volumes translated, with a commentary, by N. Bowditch (1829–1839), Hilliard, Gray, Little, and Wilkins, Publishers, Boston, MA.
- Lewis, B. M., and H. F. Hawkins, 1982: Polygonal eye walls and rainbands in hurricanes. *Bull. Amer. Meteor. Soc.*, **63**, 1294–1300.
- Lindzen, R. S., and A.-Y. Hou, 1988: Hadley circulations for zonally averaged heating centered off the equator. *J. Atmos. Sci.*, **45**, 2416–2427.
- London, J., 1996: Bernhard Haurwitz (1905–1986), A Biographical Memoir. *National Academies Press*, 85–113.
- Longuet-Higgins, M. S., 1964: Planetary waves on a rotating sphere. *Proc. Roy. Soc. A*, **279**, 446–473.
- Longuet-Higgins, M. S., 1965: Planetary waves on a rotating sphere. II. *Proc. Roy. Soc. A*, **284**, 40–68.
- Longuet-Higgins, M. S., 1968: The eigenfunctions of Laplace’s tidal equations over the sphere. *Philos. Trans. Roy. Soc. London A*, **262**, 511–607.
- Magnusdottir, G., and C.-C. Wang, 2008: Intertropical convergence zones during the active season in daily data. *J. Atmos. Sci.*, **65**, 2425–2436.
- Margules, M., 1892: Luftbewegungen in einer rotierenden Sphäroidschale bei zonaler Druckverteilung. *Sitz.-Ber. kaiserl. Akad. Wissensch. Wien, Math.-Nat. Cl., Abt. IIA*, **101**, 597–626, Translated by B. Haurwitz (1980), “Air motions in a rotating spheroidal shell with zonal pressure distributions.” NCAR Technical Note 156+STR, National Center for Atmospheric Research, Boulder, CO.
- Margules, M., 1893a: Luftbewegungen in einer rotierenden Sphäroidschale (II. Theil). *Sitz.-Ber. kaiserl. Akad. Wissensch. Wien, Math.-Nat. Cl., Abt. IIA*, **102**, 11–56, Translated by B. Haurwitz (1980), “Air motions in a rotating spheroidal shell, Part II.” NCAR Technical Note 156+STR, National Center for Atmospheric Research, Boulder, CO.
- Margules, M., 1893b: Luftbewegungen in einer rotierenden Sphäroidschale (III. Theil). *Sitz.-Ber. kaiserl. Akad. Wissensch. Wien, Math.-Nat. Cl., Abt. IIA*, **102**, 1369–1421, Translated by B. Haurwitz (1980), “Air motions in a rotating spheroidal shell, Part III.” NCAR Technical Note 156+STR, National Center for Atmospheric Research, Boulder, CO.
- Mashiko, W., 2005: Polygonal eyewall and mesovortices structure in a numerically simulated Typhoon Rusa. *SOLA*, **1**, 29–32.
- Matsuno, T., 1966: Quasi-geostrophic motions in the equatorial area. *J. Meteor. Soc. Japan*, **44**, 25–43.

- Menelaou, K., M. K. Yau, and Y. Martinez, 2013a: Impact of asymmetric dynamical processes on the structure and intensity change of two-dimensional hurricane-like annular vortices. *J. Atmos. Sci.*, **70**, 559–582.
- Menelaou, K., M. K. Yau, and Y. Martinez, 2013b: On the origin and impact of a polygonal eyewall in the rapid intensification of Hurricane Wilma (2005). *J. Atmos. Sci.*, **70**, 3839–3858.
- Möller, J. D., and R. K. Smith, 1994: The development of potential vorticity in a hurricane-like vortex. *Quart. J. Roy. Meteor. Soc.*, **120**, 1255–1265.
- Montgomery, M. T., M. Bell, S. D. Aberson, and M. Black, 2006: Hurricane Isabel (2003): New insights into the physics of intense storms. Part I: Mean vortex structure and maximum intensity estimate. *Bull. Amer. Meteor. Soc.*, **87**, 1335–1347.
- Montgomery, M. T., V. A. Vladimirov, and P. V. Denissenko, 2002: An experimental study on hurricane mesovortices. *J. Fluid Mech.*, **471**, 1–32.
- Muramatsu, T., 1986: The structure of polygonal eye of a typhoon. *J. Meteor. Soc. Japan*, **64**, 913–921.
- Naylor, J., and D. A. Schecter, 2014: Evaluation of the impact of moist convection on the development of asymmetric inner core instabilities in simulated tropical cyclones. *J. Adv. Model. Earth Syst.*, **6**, 1027–1048.
- Nieto Ferreira, R., and W. H. Schubert, 1997: Barotropic aspects of ITCZ breakdown. *J. Atmos. Sci.*, **54**, 261–285.
- Nolan, D. S., and M. T. Montgomery, 2000: The algebraic growth of wavenumber-1 disturbances in hurricane-like vortices. *J. Atmos. Sci.*, **57**, 3514–3538.
- Nolan, D. S., and M. T. Montgomery, 2002: Nonhydrostatic, three-dimensional perturbations to balanced, hurricane-like vortices. Part I: Linearized formulation, stability, and evolution. *J. Atmos. Sci.*, **59**, 2989–3020.
- Nolan, D. S., D. P. Stern, and J. A. Zhang, 2009b: Evaluation of planetary boundary layer parameterizations in tropical cyclones by comparison of in situ observations and high-resolution simulations of Hurricane Isabel (2003). Part II: Inner-core boundary layer and eyewall structure. *Mon. Wea. Rev.*, **137**, 3675–3698.
- Nolan, D. S., J. A. Zhang, and D. P. Stern, 2009a: Evaluation of planetary boundary layer parameterizations in tropical cyclones by comparison of in situ observations and high-resolution simulations of Hurricane Isabel (2003). Part I: Initialization, maximum winds, and the outer-core boundary layer. *Mon. Wea. Rev.*, **137**, 3651–3674.
- Ooyama, K., 1982: Conceptual evolution of the theory and modeling of the tropical cyclone. *J. Meteor. Soc. Japan*, **60**, 369–380.
- Peurrung, A. J., and J. Fajans, 1993: Experimental dynamics of an annulus of vorticity in a pure electron plasma. *Phys. Fluids A*, **5**, 493–499.
- Platzman, G. W., 1968: The Rossby wave. *Quart. J. Roy. Meteor. Soc.*, **94**, 225–248.
- Platzman, G. W., 1985: *Conversations with Bernhard Haurwitz*. NCAR Technical Note No. 257, Boulder, Colorado, 184 pp.
- Platzman, G. W., 1996: The S-1 chronicle: A tribute to Bernhard Haurwitz. *Bull. Amer. Meteor. Soc.*, **77**, 1569–1577.
- Rogers, R. F., and Coauthors, 2017: Rewriting the tropical record books: The extraordinary intensification of Hurricane Patricia (2015). *Bull. Amer. Meteor. Soc.*, **98**, 2091–2112.
- Rossby, C.-G., 1939: Relation between variations in the intensity of the zonal circulation of the atmosphere and the displacements of the semi-permanent centers of action. *J. Mar. Res.*, **2**, 38–55.
- Rossby, C.-G., 1940: Planetary flow patterns in the atmosphere. *Quart. J. Roy. Meteor. Soc.*, **66**, Supplement.
- Rozoff, C. M., J. P. Kossin, W. H. Schubert, and P. J. Mulero, 2009: Internal control of hurricane intensity variability: The dual nature of potential vorticity mixing. *J. Atmos. Sci.*, **66**, 133–147.
- Rozoff, C. M., W. H. Schubert, B. D. McNoldy, and J. P. Kossin, 2006: Rapid filamentation zones in intense tropical cyclones. *J. Atmos. Sci.*, **63**, 325–340.

- Schneider, E. K., 1977: Axially symmetric steady state models of the basic state for instability and climate studies. Part II. Nonlinear calculations. *J. Atmos. Sci.*, **34**, 280–296.
- Schneider, E. K., and R. S. Lindzen, 1977: Axially symmetric steady state models of the basic state for instability and climate studies. Part I. Linear calculations. *J. Atmos. Sci.*, **34**, 253–279.
- Schubert, W. H., and B. T. Alworth, 1987: Evolution of potential vorticity in tropical cyclones. *Quart. J. Roy. Meteor. Soc.*, **113**, 147–162.
- Schubert, W. H., P. E. Ciesielski, D. E. Stevens, and H.-C. Kuo, 1991: Potential vorticity modeling of the ITCZ and the Hadley circulation. *J. Atmos. Sci.*, **48**, 1493–1509.
- Schubert, W. H., M. T. Montgomery, R. K. Taft, T. A. Guinn, S. R. Fulton, J. P. Kossin, and J. P. Edwards, 1999: Polygonal eyewalls, asymmetric eye contraction, and potential vorticity mixing in hurricanes. *J. Atmos. Sci.*, **56**, 1197–1223.
- Schubert, W. H., C. M. Rozoff, J. L. Vigh, B. D. McNoldy, and J. P. Kossin, 2007: On the distribution of subsidence in the hurricane eye. *Quart. J. Roy. Meteor. Soc.*, **133**, 595–605.
- Simpson, R. H., and L. G. Starrett, 1955: Further studies of hurricane structure by aircraft reconnaissance. *Bull. Amer. Meteor. Soc.*, **36**, 459–468.
- Slocum, C. J., G. J. Williams, R. K. Taft, and W. H. Schubert, 2014: Tropical cyclone boundary layer shocks. *arXiv:1405.7939 [physics.ao-ph]*, 19 pp.
- Smith, R. K., and S. Vogl, 2008: A simple model of the hurricane boundary layer revisited. *Quart. J. Roy. Meteor. Soc.*, **134**, 337–351.
- Stern, D. P., and D. S. Nolan, 2012: On the height of the warm core in tropical cyclones. *J. Atmos. Sci.*, **69**, 1657–1680.
- Stern, D. P., and F. Zhang, 2013: How does the eye warm? Part I: A potential temperature budget analysis of an idealized tropical cyclone. *J. Atmos. Sci.*, **70**, 73–90.
- Swarztrauber, P. N., and A. Kasahara, 1985: The vector harmonic analysis of Laplace's tidal equations. *SIAM Journal on Scientific and Statistical Computing*, **6**, 464–491.
- Wang, C.-C., and G. Magnusdottir, 2005: ITCZ breakdown in three-dimensional flows. *J. Atmos. Sci.*, **62**, 1497–1512.
- Wang, C.-C., and G. Magnusdottir, 2006: The ITCZ in the central and eastern Pacific on synoptic time scales. *Mon. Wea. Rev.*, **134**, 1405–1421.
- Wang, H., J. P. Boyd, and R. A. Akmaev, 2016: On computation of Hough functions. *Geosci. Model Dev.*, **9**, 1477–1488.
- Wang, Y., 2008: Rapid filamentation zone in a numerically simulated tropical cyclone. *J. Atmos. Sci.*, **65**, 1158–1181.
- Wang, Y., 2009: How do outer spiral rainbands affect tropical cyclone structure and intensity? *J. Atmos. Sci.*, **66**, 1250–1273.
- Williams, G. J., R. K. Taft, B. D. McNoldy, and W. H. Schubert, 2013: Shock-like structures in the tropical cyclone boundary layer. *J. Adv. Model. Earth Syst.*, **5**, 338–353.
- Wingo, S. M., and K. R. Knupp, 2016: Kinematic structure of mesovortices in the eyewall of Hurricane Ike (2008) derived from ground-based dual-Doppler analysis. *Mon. Wea. Rev.*, **144**, 4245–4263.
- Wu, C. C., S. N. Wu, H. H. Wei, and S. F. Abarca, 2016: The role of convective heating in tropical cyclone eyewall ring evolution. *J. Atmos. Sci.*, **73**, 319–330.
- Yau, M. K., Y. Liu, D.-L. Zhang, and Y. Chen, 2004: A multiscale numerical study of Hurricane Andrew (1992). Part VI: Small-scale inner-core structures and wind streaks. *Mon. Wea. Rev.*, **132**, 1410–1433.
- Žagar, N., A. Kasahara, K. Terasaki, J. Tribbia, and H. Tanaka, 2015: Normal-mode function representation of global 3-D data sets: Open-access software for the atmospheric research community. *Geosci. Model Dev.*, **8**, 1169–1195.
- Zhang, D.-L., Y. Liu, and M. K. Yau, 2002: A multiscale numerical study of Hurricane Andrew (1992). Part V: Inner-core thermodynamics. *Mon. Wea. Rev.*, **130**, 2745–2763.